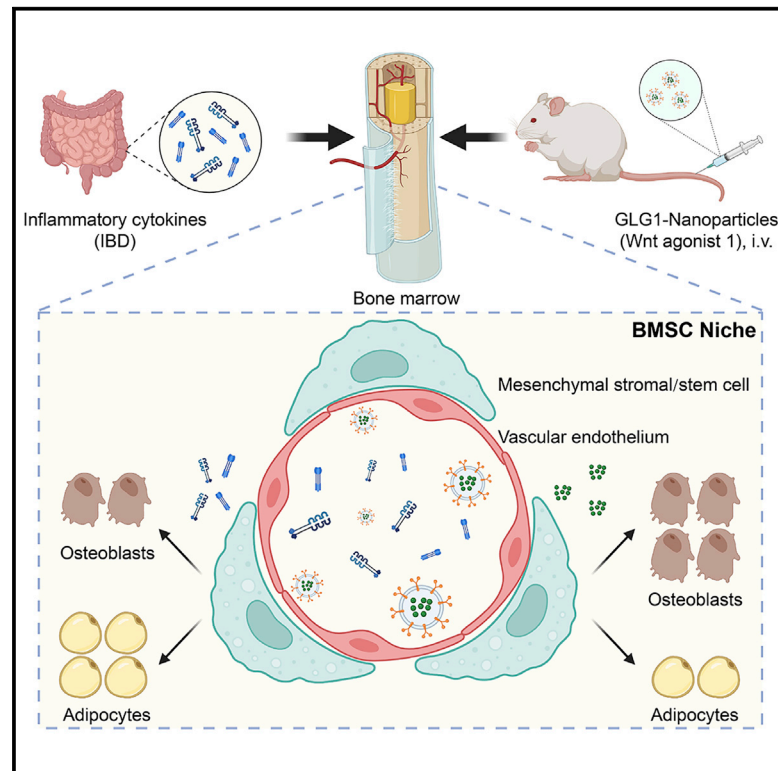**Article**

Exosome-based bone-targeting drug delivery alleviates impaired osteoblastic bone formation and bone loss in inflammatory bowel diseases

Graphical abstract

Authors

Jiawei Guo, Fuxiao Wang, Yan Hu, ..., Can Xu, Xiao Chen, Jiacan Su

Correspondence

xxcc211@126.com (C.X.),
sirchenxiao@126.com (X.C.),
drsujiacan@163.com (J.S.)

In brief

Impaired osteoblastic bone formation contributes to reduced bone mass and increased fracture risks complicated with inflammatory bowel diseases (IBDs). Guo et al. demonstrate that exosomes genetically modified with Golgi glycoprotein 1 target bone and direct BMSC fate toward osteogenic lineage, serving as a promising anabolic therapy for IBD-related skeletal disorders.

Highlights

- Impaired osteoblastic bone formation leads to reduced bone mass and quality in IBD

- Systematic inflammation inhibits osteogenic differentiation of BMSCs

- Bone-targeted therapy by exosomes is applicable for inflammatory skeletal disorders

CellPress

Article

Exosome-based bone-targeting drug delivery alleviates impaired osteoblastic bone formation and bone loss in inflammatory bowel diseases

Jiawei Guo,[1,2,5] Fuxiao Wang,[1,5] Yan Hu,[1,5] Ying Luo,[2] Yan Wei,[1] Ke Xu,[1] Hao Zhang,[1] Han Liu,[1] Lumin Bo,[3] Shunli Lv,[3] Shihao Sheng,[2] Xinchen Zhuang,[2] Tao Zhang,[2] Can Xu,[3,*] Xiao Chen,[2,*] and Jiacan Su[1,2,4,6,*]

[1]Institute of Translational Medicine, Shanghai University, Shanghai 200444, China
[2]Department of Orthopedics Trauma, Shanghai Changhai Hospital, Naval Medical University, Shanghai 200433, China
[3]Department of Gastroenterology, Shanghai Changhai Hospital, Naval Medical University, Shanghai 200433, China
[4]Organoid Research Center, Shanghai University, Shanghai 200444, China
[5]These authors contributed equally
[6]Lead contact
*Correspondence: xxcc211@126.com (C.X.), sirchenxiao@126.com (X.C.), drsujiacan@163.com (J.S.)
https://doi.org/10.1016/j.xcrm.2022.100881

SUMMARY

Systematic bone loss is commonly complicated with inflammatory bowel diseases (IBDs) with unclear pathogenesis and uncertain treatment. In experimental colitis mouse models established by dextran sulfate sodium and *IL-10* knockout induced with piroxicam, bone mass and quality are significantly decreased. Colitis mice demonstrate a lower bone formation rate and fewer osteoblasts in femur. Bone marrow mesenchymal stem/stromal cells (BMSCs) from colitis mice tend to differentiate into adipocytes rather than osteoblasts. Serum from patients with IBD promotes adipogenesis of human BMSCs. RNA sequencing reveals that colitis downregulates Wnt signaling in BMSCs. For treatment, exosomes with Golgi glycoprotein 1 inserted could carry Wnt agonist 1 and accumulate in bone via intravenous administration. They could alleviate bone loss, promote bone formation, and accelerate fracture healing in colitis mice. Collectively, BMSC commitment in inflammatory microenvironment contributes to lower bone quantity and quality and could be rescued by redirecting differentiation toward osteoblasts through bone-targeted drug delivery.

INTRODUCTION

Systematic bone loss is commonly complicated with chronic inflammation, which is exemplified in various diseases like rheumatic arthritis, asthma, and nephritis.[1] Chronic gastrointestinal diseases are closely associated with skeletal disorders, which have not been fully investigated.[2] Among them, inflammatory bowel diseases (IBDs), mainly comprising ulcerative colitis (UC) and Crohn's disease, have emerged as an intractable challenge with increased morbidity worldwide in the past decades.[3] The prevalence in the Western world is up to 0.5% of the general population, while in China, it is estimated to be 13/100,000.[4,5] Meanwhile, the occurrence of osteopenia and osteoporosis in patients with IBD can be as high as 67% and 57.6%, respectively,[6] which is in part due to bone mineral loss caused by steroid treatment. Furthermore, it is independent of the application of glucocorticoid, used in controlling active IBD, since osteoporosis presents and develops before the application.[7] Accordingly, bone loss directly results in fragility, with robust evidence showing that the relative fracture risk rises to about 1.3- to 1.4-fold.[6,8] Calcium and vitamin D supplementation are

recommended for bone mineral density (BMD) maintenance for patients with IBD according to the guidelines.[9,10] However, the skeletal alterations in patients with IBD remain ambiguous, calling for further explorations.

Bone turnover includes bone resorption and subsequent coupled bone formation.[11–13] As yet, studies have illustrated that bone resorption increased pathologically in IBDs, evidenced by osteoclast overactivation.[14,15] Meanwhile, few studies reported bone formation.[16,17] Clinically, osteoporosis in IBDs has been treated mainly by antiresorptive drugs, including bisphosphonates and denosumab, but the safety and efficacy concerns have limited their applications. In recent years, anabolic therapies represented by parathyroid hormone analog and sclerostin monoclonal antibody are attached to great importance.[18–22] The investigation of osteogenesis and the development of anabolic therapy are needed in the treatment of bone loss in IBDs.[11,23]

Osteoblastic bone formation is mediated by bone marrow mesenchymal stromal/stem cell (BMSCs), the common progenitor of osteoblasts and adipocytes.[24] They adhere to vascular endothelium to constitute the BMSC niche.[25,26] In IBDs,
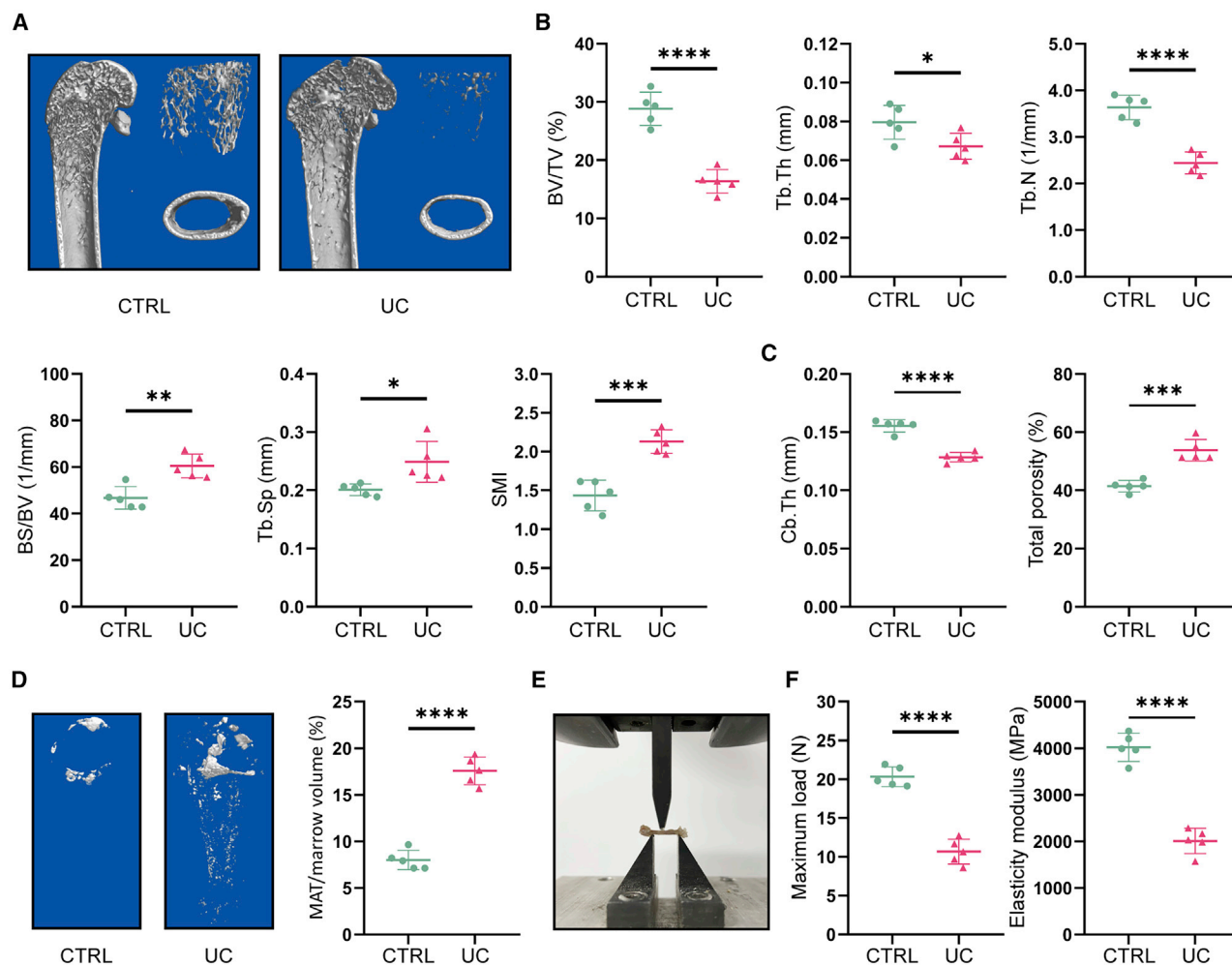
Figure 1. UC models showed reduced bone mass but increased bone marrow adipose

(A) Representative μCT reconstruction images of the femurs. Overall view (left), trabecular bone (right, upper), cortical bone (right, lower). n = 5.

(B) Quantitative analysis of the trabecular bone including BV/TV, Tb.Th, Tb.N, BS/BV, Tb.Sp, and SMI. n = 5.

(C) Quantitative analysis of the cortical bone including cortical bone thickness (Cb.Th) and total porosity. n = 5.

(D) Representative μCT reconstruction images of the bone marrow adipose tissue. Marrow adipose tissue/marrow volume as a quantitative measurement. n = 5.

(E) Image of mechanical stress testing.

(F) Maximum load and elasticity modulus of the femurs. n = 5.

Data are represented as mean ± SD (error bars) from biological replicates. *$p < 0.05$, **$p < 0.01$, ***$p < 0.001$, ****$p < 0.0001$, by non-paired Student's t test. See also Figures S1–S3.

increased inflammatory factors like tumor necrosis factor α (TNF-α) and interleukin-1β (IL-1β) could harm the BMSC niche by suppressing its proliferation and function to impair bone formation, leading to reduced bone mass and quality, along with adipose tissue accumulation.[27–30] Pharmacologically, the proliferation and osteogenesis could be rescued by targeted drug delivery to BMSCs.[31,32] Therefore, targeting BMSCs is a feasible strategy to correct its commitment and promote osteoblastogenesis in IBDs.[33]

Exosomes, as natural extracellular vesicles with ideal biocompatibility and stability, can be genetically modified to target the BMSC niche as nanocarriers based on receptor-ligand interaction.[34–36] E-selectin expressed in the bone vascular niche promotes the bone metastasis of cancer cells,

which is mediated by Golgi glycoprotein 1 (GLG1), the ligand of E-selectin.[37] Based on our previous study, bone-targeted exosomes could be obtained by genetically modifying surface-specific ligands. By applying the CXCR4-SDF1 axis mediating hematopoietic stem cell homing and tumor bone metastasis, engineered CXCR4+ exosomes loading the antago-miR-188 could accumulate in the bone marrow to treat age-related bone loss.[35]

In this study, we investigated the bone formation capacity, the BMSC differentiation tendency, and the underlying molecular mechanisms in two IBD models, and we constructed GLG1-modified exosomes to target the BMSC niche, delivering Wnt agonist 1 to rescue BMSC commitment and osteoblastic bone formation.
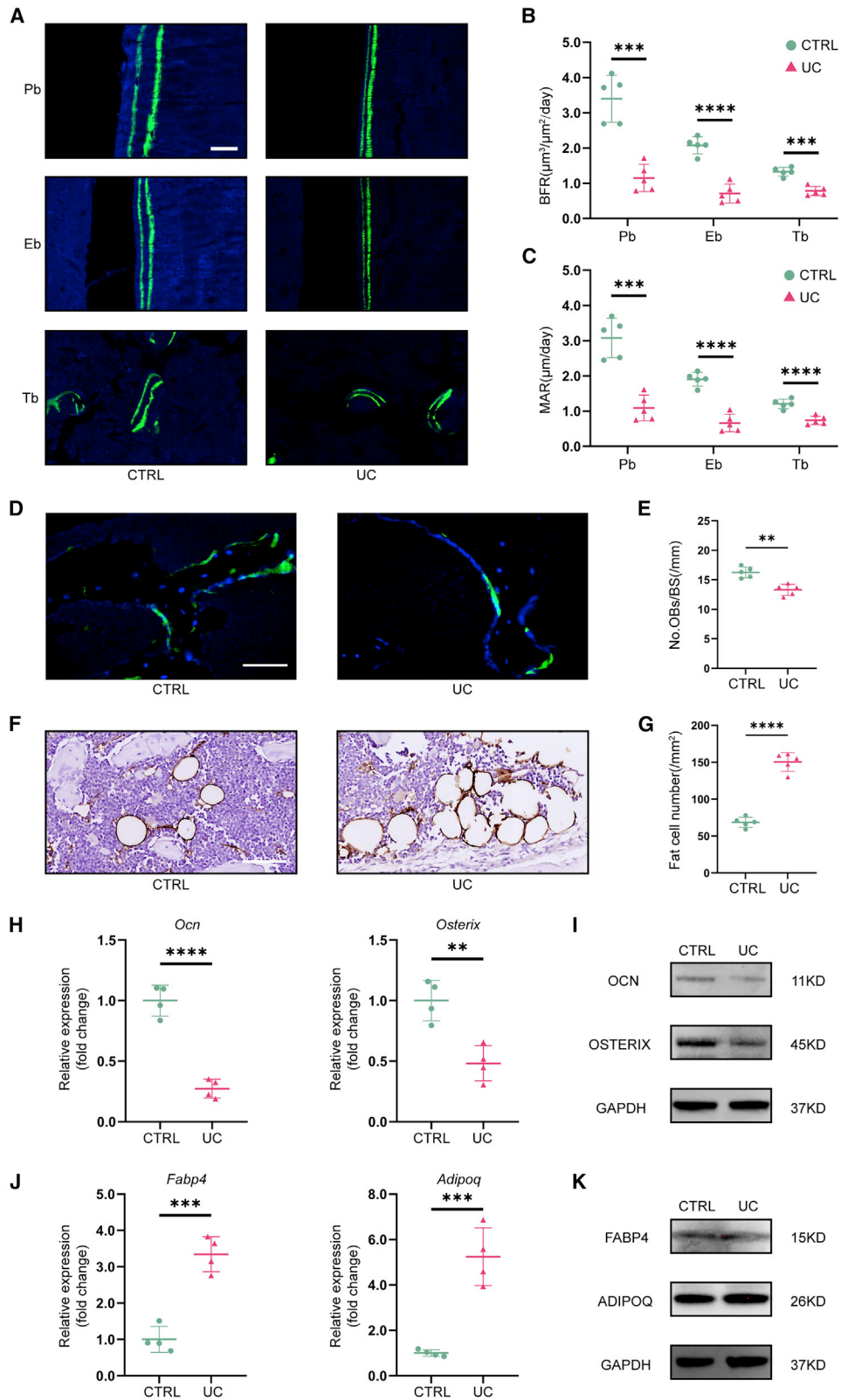
RESULTS

UC mice showed reduced bone mass and accumulated bone marrow fat

To testify if the bone mass is reduced in IBD mice, we first established the UC model with dextran sulfate sodium (DSS) as previously reported.[14,38] Compared with the control, mice in the experimental group had a shorter colon (Figure S1A). Inflammatory cell infiltration, epithelial destruction, and gland abnormity were observed in hematoxylin and eosin (H&E) staining (Figure S1B). Mice exhibited significant weight loss and increased disease activity index (DAI) (Figures S1C and S1D). Blood tests showed that the serum level of albumin, vitamin D, and alkaline phosphatase (ALP) of UC mice was decreased, while 5-hydroxytryptamine was increased. Besides, calcium and phosphate variations did not show statistical significance (Figures S1E–S1J). For the skeletal alterations, the representative micro-computed tomography (μCT) images of the femurs were shown (Figure 1A). For trabecular bone, UC mice had lower bone mass, verified by lower bone volume fraction (BV/TV), trabecular thickness (Tb.Th), and trabecular number (Tb.N), as well as higher bone surface/BV ratio (BS/BV), trabecular separation (Tb.Sp) and structure model index (SMI) (Figure 1B). Consistently, H&E staining showed the reduced trabecular area and greater fat cell density (Figures S1K–S1M). For cortical bone, UC mice had lower cortical bone thickness (Cb.Th) and higher porosity (Figure 1C). Osmium tetroxide staining showed remarkable bone marrow adipose tissue accumulation in UC mice compared with control mice (Figure 1D). For bone quality evaluation, mechanical stress testing was applied, and the results showed that the femurs of UC mice had lower maximum load and elasticity modulus (Figures 1E and 1F). The Goldner's trichrome staining showed reduced osteoid formation (Figures S1N–S1Q), and the tartrate-resistant phosphatase (TRAP) staining showed increased osteoclasts in UC mice (Figures S1R and S1S).

Next, we established piroxicam-induced colitis in *IL-10*$^{-/-}$ mice, another UC model.[39] Their colons were shorter than their wild-type (WT) littermates (Figure S2A). H&E staining showed remarkable inflammation within the colons (Figure S2B). Weight loss and DAI elevation were significant (Figures S2C and S2D). μCT results showed that femurs of *IL-10*$^{-/-}$ mice exhibited lower BV/TV, Tb.Th, Tb.N, Cb.Th, and porosity and higher BS/BV and Tb.Sp. SMI of *IL-10*$^{-/-}$ mice was higher but with no statistical significance (Figures S2E–S2G). H&E staining showed decreased trabecular area but increased fat cell density in *IL-10*$^{-/-}$ mice (Figures S2H–S2J). Mechanical stress testing demonstrated decreased maximum load and elasticity modulus of the femurs in *IL-10*$^{-/-}$ mice compared with WT littermates (Figures S2K and S2L). Moreover, we established a chronic UC model, and μCT examinations showed consistent results in trabecular and cortical bone (Figures S3A–S3C).

UC mice exhibited reduced osteogenesis and increased adipogenesis in bone marrow

To explore the bone formation capacity, we first performed a calcein double-labeling assay. In the DSS-induced UC mice, results showed that the bone formation rate (BFR) and mineral apposition rate (MAR) were significantly decreased in the femurs compared with the control group (Figures 2A–2C), and similar results were observed in *IL-10*$^{-/-}$ mice and chronic colitis mice (Figures S3D–S3F and S4A–S4C). Immunofluorescence (IF) staining of osteocalcin (OCN) showed fewer positive osteoblasts, while immunohistochemistry (IHC) staining of fatty-acid-binding protein 4 (FABP4) showed significantly increased adipocytes in the femur of UC mice and *IL-10*$^{-/-}$ mice (Figures 2D–2G and S4D–S4G). Furthermore, quantitative real-time PCR and western blotting showed that the expression of *Ocn* and *Osterix* were significantly inhibited in UC mice (Figures 2H and 2I), whereas the expression of *Fabp4* and *Adipoq* was significantly increased in UC mice (Figures 2J and 2K).

BMSCs from UC mice and patients shifted from osteogenic to adipogenic differentiation

Next, we investigated if local inflammation affected BMSC differentiation in UC. Various inflammatory cytokines including IL-1α, IL-1β, TNF-α, IL-6, and IL-33 increased transcriptionally in the bone marrow of UC mice (Figures 3A, S5A, and S5B). Myeloid elf-1 like factor, known to inhibit osteogenic but stimulate adipogenic differentiation of BMSCs, also elevated transcriptionally (Figure S5C).[40,41] Then, we isolated BMSCs. The colony-forming unit fibroblast (CFU-F) assay revealed that BMSCs from UC mice formed fewer colonies than the control mice (Figure 3B). Subsequently, we induced osteogenesis and adipogenesis of BMSCs *in vitro*. Alizarin red S staining, ALP staining, and von Kossa staining demonstrated the impaired osteogenic potential of BMSCs, evidenced by less calcium deposition and ALP (Figures 3C, S5D, and S5E).

Figure 2. UC models showed suppressed osteogenesis but promoted adipogenesis *in vivo*

(A) Representative images of calcein double-labeling assay of periosteum bone (Pb), endosteal bone (Eb), and trabecular bone (Tb) of the femurs. n = 5. Scale bar, 50 μm.

(B and C) Bone formation rate (BFR) per bone surface and mineral apposition rate (MAR) of the femurs. n = 5.

(D) Immunofluorescence staining of OCN (green) of the femurs. n = 5. Scale bar, 50 μm.

(E) Quantitative analysis of OCN$^+$ osteoblast number per bone surface (No.OBs/BS). n = 5.

(F) Immunohistochemistry staining of FABP4 (gray) of the femurs. n = 5. Scale bar, 50 μm.

(G) Quantitative analysis of FABP4$^+$ fat cell number. n = 5.

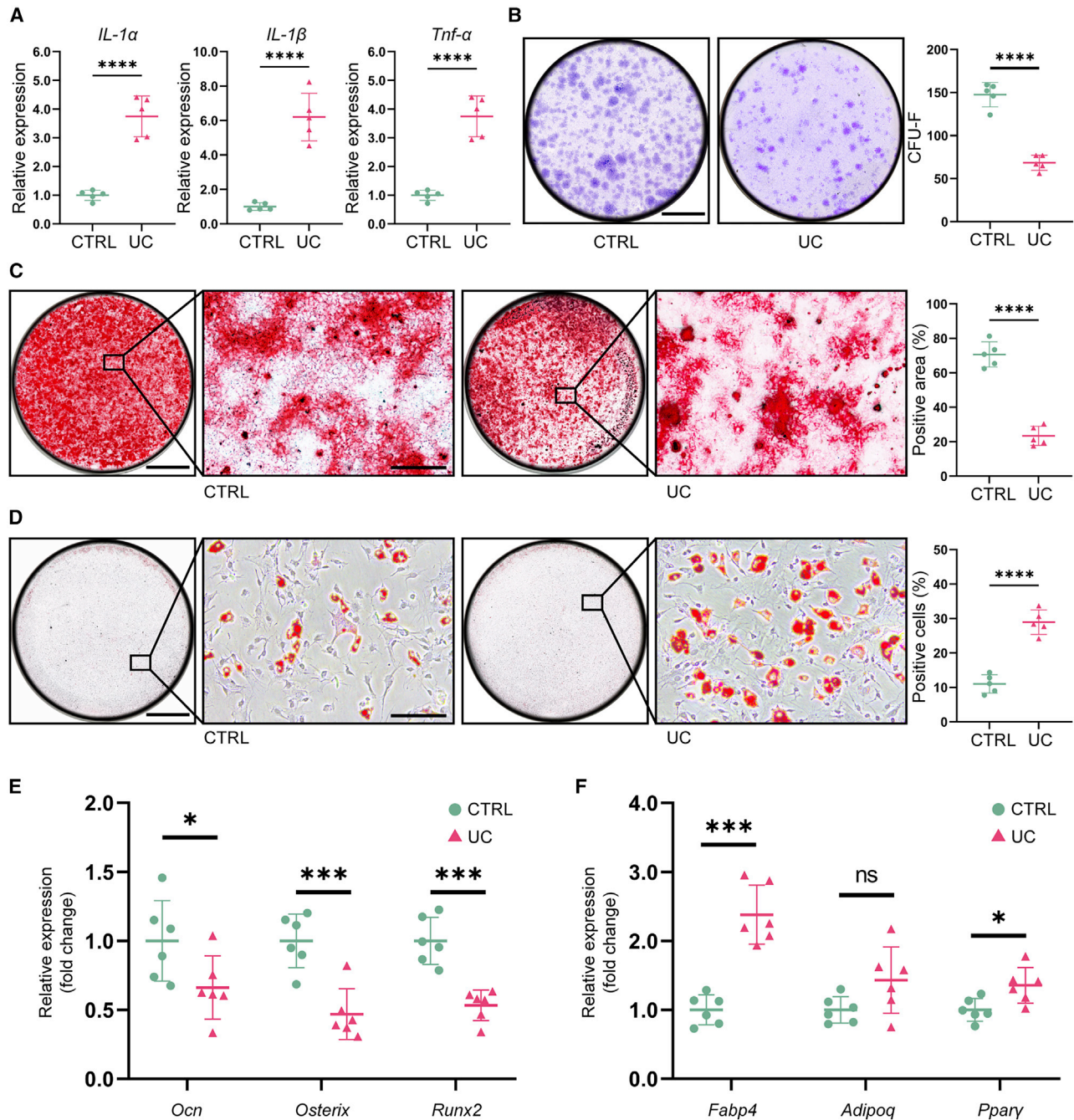(H) *Ocn* and *Osterix* mRNA expressions. n = 5.

(I) *Ocn* and *Osterix* protein levels. n = 5.

(J) *Fabp4* and *Adipoq* mRNA expressions. n = 5.

(K) *Fabp4* and *Adipoq* protein levels. n = 5.

Data are represented as mean ± SD (error bars) from biological replicates. **p < 0.01, ***p < 0.001, ****p < 0.0001, by non-paired Student's t test.

See also Figures S2–S4.

Figure 3. Inflammation in UC inhibited the proliferation of BMSC *in vitro*

(A) *IL-1α*, *IL-1β*, and *Tnf-α* mRNA expressions. n = 5.

(B) Representative images of colony-forming unit fibroblast (CFU-F) assay of BMSC. Colony number as quantitative measurements. n = 5. Scale bar, 500 μm.

(C) Representative images of alizarin red S staining of BMSCs after 14 day osteogenic induction. Positive cells as quantitative measurements. n = 5. Scale bars, 500 μm (left) and 50 μm (right).

(D) Representative images of oil red staining of BMSCs after 21 day adipogenic induction. Positive cells as quantitative measurements. n = 5. Scale bars, 500 μm (left) and 50 μm (right).

(E) *Ocn*, *Osterix*, and *Runx2* mRNA expressions of human BMSCs after 7 day osteogenic induction, with simultaneous treatment of the serum from health volunteers (control group) and patients with UC (UC group), respectively. n = 6.

(F) *Fabp4*, *Adipoq*, and *Pparγ* mRNA expressions of human BMSCs after 7 day adipogenic induction, with simultaneous treatment of the serum from health volunteers (control group) and patients with UC (UC group), respectively. n = 6.

Data are represented as mean ± SD (error bars) from biological replicates. ns, not significant, *p < 0.05, ***p < 0.001, ****p < 0.0001, by non-paired Student's t test. See also Figure S5.
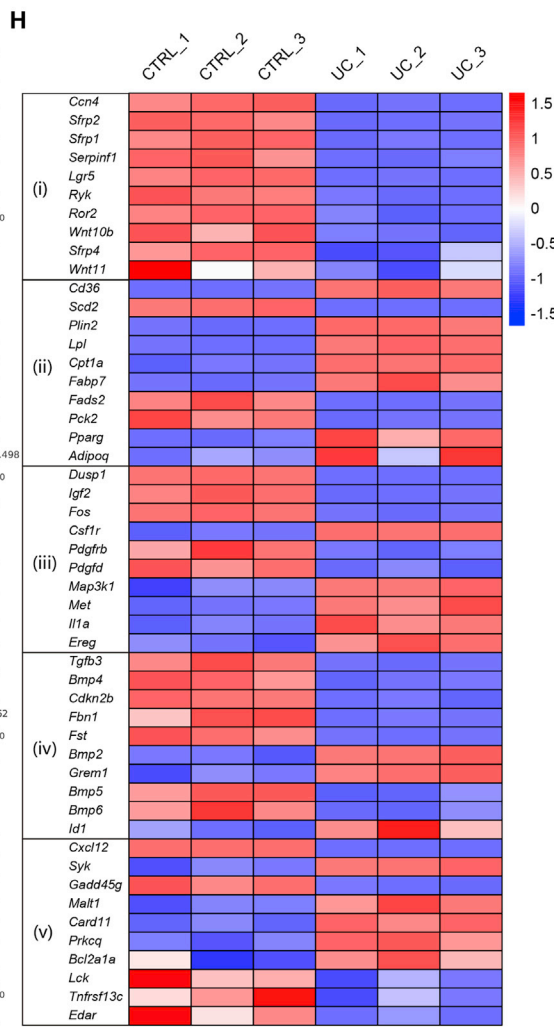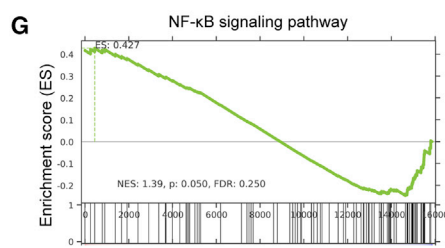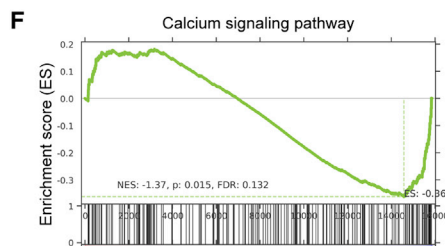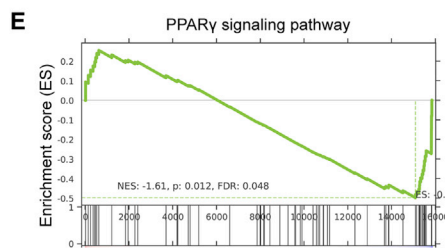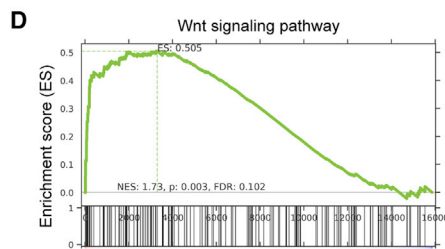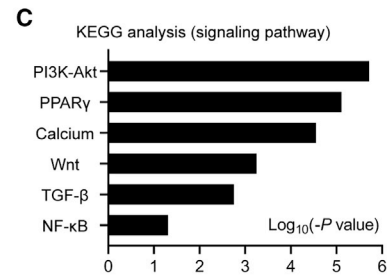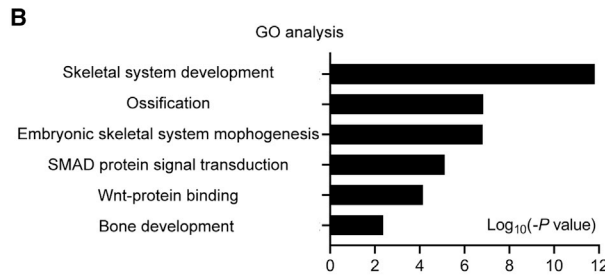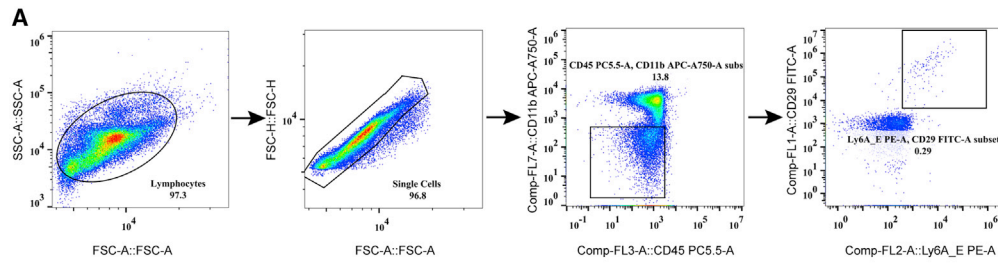
(legend on next page)

Conversely, the adipogenic differentiation was significantly enhanced by oil red staining (Figure 3D). We obtained human BMSCs from fractured patients and cultured it with serum from either healthy volunteers or patients with UC to evaluate the effects of the pathological microenvironment of IBDs on BMSCs in vitro. After osteogenic induction, the relative expression of osteoblastic genes, including Ocn, Osterix, and Runx2, were decreased notably, while adipogenic genes, including Fabp4 and Ppary, were upregulated with the serum culture from patients with UC (Figures 3E and 3F).

RNA sequencing revealed inhibited osteogenic but increased adipogenic pattern of gene expression in UC mice

To reveal the pathogenesis of bone loss in UC at the molecular level, we isolated BMSCs by fluorescence-activated cell sorting (FACS). The BMSC was described as Ly6A/E$^+$CD29$^+$CD45$^-$CD11b$^-$ (Figure 4A).[42] Then, we performed RNA sequencing (RNA-seq). According to the analysis of the differently expressed genes, 704 genes were upregulated, while 993 genes were downregulated, in UC. GO analysis indicated that downregulated genes by UC were enriched in the Wnt signaling pathway, osteoblast differentiation, and Wnt-protein binding. The upregulated genes were enriched mainly in the immune system process (data not shown). As for the skeletal system, differently expressed genes were enriched in ossification or Wnt-protein binding, etc. (Figure 4B). Moreover, KEGG analysis indicated that UC notably influenced development and regeneration and lipid metabolism (data not shown). Specifically, the Ppary and Wnt signaling pathways, critical to BMSC differentiation, were significantly affected by UC (Figure 4C). Gene set enrichment analysis (GSEA) revealed that the signature genes for Wnt signaling were downregulated, but those for Ppary signaling were upregulated, in UC (Figures 4D and 4E). Besides, the signature genes for the calcium signaling pathway were upregulated as well, but those for the nuclear factor κB (NF-κB) signaling pathway were downregulated with a marginal significance (Figures 4F and 4G). To identify the gene transcription alterations involved in BMSC fate, we assessed the related gene expressions in Wnt, Ppary, MAPK, TGF-β, and NF-κB signaling pathways. Most critical genes for osteoblast maturation, such as Wnt10b and Wnt11, were downregulated by UC in the Wnt signaling pathway. Likewise, most of the important genes for adipogenesis, such as Lpl, Pparg, and Adipoq, were upregulated by UC. Meanwhile, the other pathways were also affected by UC to various degrees (Figure 4H).

TNF-α suppressed the Wnt/β-catenin signaling pathway in osteogenesis

Crucial to osteogenesis, the Wnt signaling pathway was significantly suppressed in BMSCs from UC mice. TNF-α has been re-

garded as a master cytokine in human IBDs (Figure 3A).[6] To explore the molecular mechanisms, we first treated BMSCs with recombinant TNF-α in vitro and performed co-immunoprecipitation. Results showed that p50 could directly bind to β-catenin, but the interaction was blocked with TNF-α treatment (Figure 5A). Immunoblotting showed β-catenin was dramatically reduced, while phosphate IKKβ and phosphate p50 were increased, by TNF-α treatment (Figure 5B). To determine whether TNF-α affects the transcriptional activity of Wnt/β-catenin signaling, we transfected TOPFlash luciferases reporter vectors into BMSCs and found that the promoted TOPFlash reporter activity by the agonist of the Wnt pathway was significantly inhibited by TNF-α (Figure 5C). Then, we suspected that the reduced β-catenin was attributed to degradation mediated by ubiquitination.[43] Indeed, TNF-α treatment substantially promoted β-catenin ubiquitylation in a dose-dependent manner (Figure 5D). Next, we investigated β-catenin degradation by cycloheximide chasing assay, verifying that β-catenin degradation was accelerated by TNF-α treatment (Figure 5E). Further, we demonstrated significantly decreased β-catenin in both cytosol and nucleus with TNF-α treatment (Figure 5F). The chromatin immunoprecipitation assay showed that the recruitment of β-catenin to the promoters of Runx2 and Osterix was inhibited with TNF-α treatment (Figures 5G and 5H).

Preparation of bone-targeted and drug-loaded nanoparticles

Given that the Wnt/β-catenin signaling pathway was downregulated in BMSCs of UC, we developed bone-targeted drug-loaded nanoparticles (NPs) to activate the suppressed Wnt signaling. GLG1 was reported vital for prostate cancer cells metastasizing to bone.[37] Employing that strategy, we constructed a GLG1-overexpressed NIH/3T3 cell line as our previous study.[35] Then, we collected GLG1 exosomes and loaded them with the Wnt agonist 1 by cyclic extrusion to produce the bone-targeted NP (GLG1-NP) for drug delivery (Figure 6A). The transmission electron microscope and NP tracking analysis revealed that the NPs maintained the morphology of exosomes (Figures 6B and 6C). Western blotting showed that the NPs had exosome markers like CD9, HSP70, TSG101, and CD63 and the GLG1-NP had more GLG1 (Figure 6D). To testify if the GLG1-NP could target bone in vivo, we treated the mice with the Cy5-labeled NP intravenously and performed biophotonic imaging analysis. The results demonstrated that the Cy5-labeled NPs were mainly enriched in the liver, and the GLG1-NP accumulated in the femur in a time-dependent manner (Figure 6E).

GLG1-NP pharmacologically rescued osteoblastic bone formation in UC

Furthermore, we tested if the bone-targeted drug-loaded GLG1-NP could rescue the bone loss in DSS-induced UC by promoting

Figure 4. Wnt signaling was inhibited in BMSCs from UC models
(A) The sorting strategy of BMSCs by flow cytometry. The BMSC is described as the cluster whose expression pattern is Ly6A/E$^+$CD29$^+$CD45$^-$CD11b$^-$.
(B and C) The RNA sequencing results of sorted BMSCs. GO and KEGG analysis of differently expressed genes between BMSCs from control and UC mice. n = 3.
(D–G) GSEA revealing the enrichment of differently expressed genes in the Wnt (D), Ppary (E), calcium (F), and NF-κB (G) signaling pathways, respectively. n = 3.
(H) The heatmap based on the differently expressed genes between BMSCs from control and UC mice. Representative genes in the Wnt pathway (i), PPARγ (ii), MAPK (iii), TGF-β (iv), and NF-κB pathway are plotted. n = 3. Data were obtained from biological replicates.
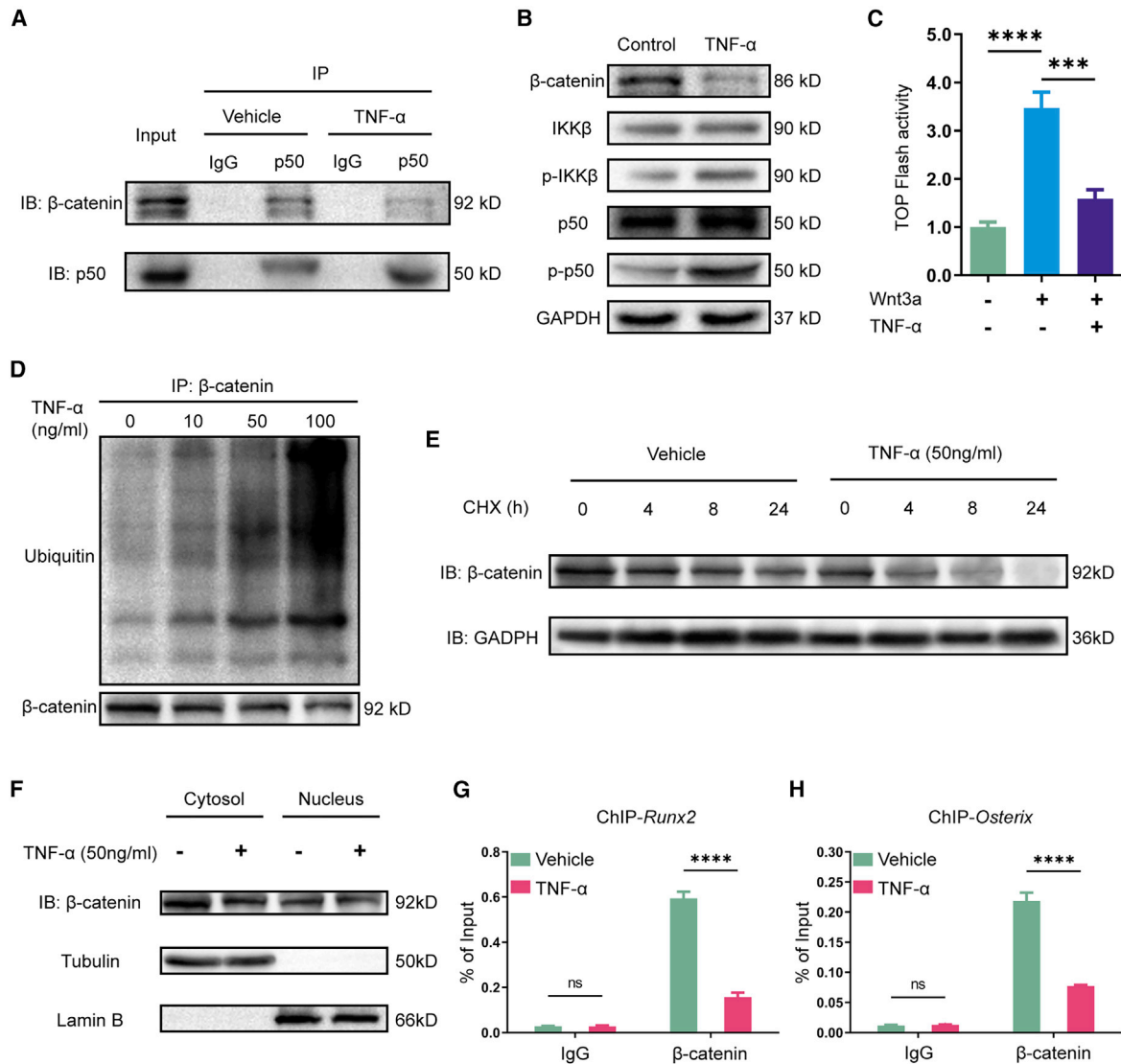
Figure 5. TNF-α promoted β-catenin degradation and inhibited osteogenic gene expression

(A) Co-immunoprecipitation of BMSCs treated by vehicle or recombinant TNF-α.

(B) Immunoblotting of downstream molecules of the Wnt and NF-κB signaling pathways in BMSCs after vehicle or recombinant TNF-α treatment.

(C) Luciferase reporter assay. BMSC was transfected with β-catenin expression plasmid with TOPFlash reporter. Firefly luciferase activities were measured.

(D) Immunoblotting of β-catenin and the presence of ubiquitin.

(E) Cycloheximide chasing assay of β-catenin in BMSCs after being treated by vehicle or recombinant TNF-α for 24 h.

(F) Immunoblotting of β-catenin in the cytoplasm and nucleus of BMSCs, which were treated by vehicle or recombinant TNF-α for 24 h.

(G and H) Chromatin immunoprecipitation (ChIP) assays on the promoter regions of the *Runx2* and *Osterix* genes were performed in BMSCs treated by vehicle or recombinant TNF-α for 24 h. n = 3.

Data are represented as mean ± SD (error bars) from biological replicates. ns, not significant, ****$p < 0.0001$, by paired Student's t test.

bone formation. The UC mice were treated with GLG1-NP for 2 weeks, with GLG1+ exosomes containing vehicle regarded as the control (Figure 7A). Above all, GLG1-NP did not demonstrate notable toxicity to vital organs including the heart, liver, spleen, lung, and kidney (data not shown), and GLG1-NP treatment did not affect the body weight changes, DAIs, and colon inflammations of UC mice (data not shown). But GLG1-NP significantly increased BV as evidenced by elevated BV/TV and Cb.Th in UC mice (Figures 7B–7D). Tb.Th, Tb.N, BS/BV, Tb.Sp, SMI,

and porosity were improved by GLG1-NP (Figures S6A and S6B). Besides, GLG1-NP alleviated bone marrow adipose accumulation in UC mice (Figures S6C and S6D). Moreover, the maximum load and elasticity of the femurs of UC mice were increased by GLG1-NP (Figures S6E and S6F). BFR and MAR were also higher in UC mice treated with GLG1-NP than in the vehicle-treated ones (Figures 7E–7G). Additionally, there were more OCN+ osteoblasts and fewer FABP4+ adipocytes in UC mice treated with GLG1-NP (Figures 7H and 7I).
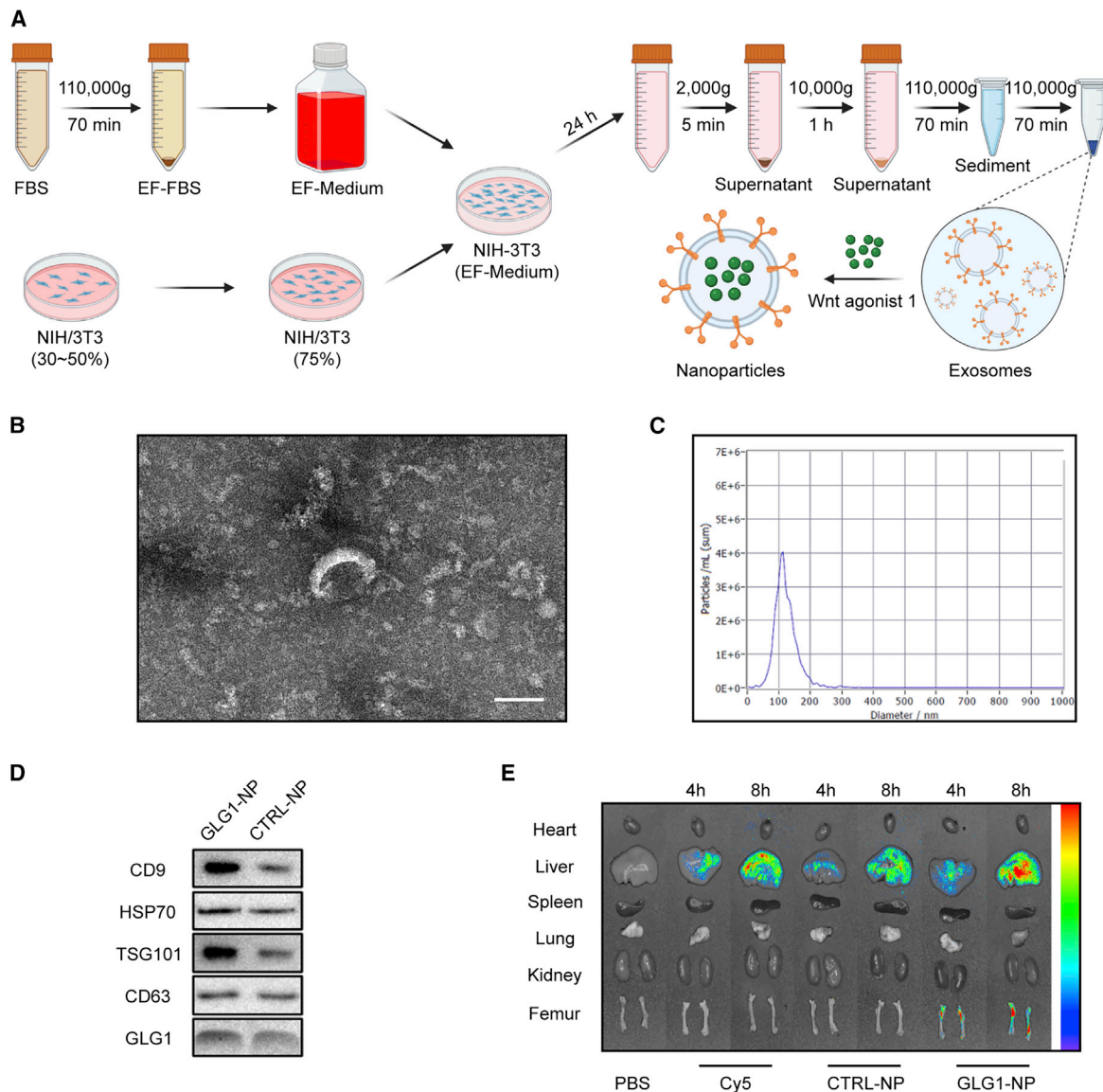
Figure 6. Preparation of bone-targeted and drug-loaded nanoparticles

(A) Schematic diagram of exosome isolation including cell culture, gradient centrifugation, and drug (Wnt agonist 1) loading.

(B) Morphological image of the NP revealed by transmission electron microscope.

(C) Diameter distribution of the NP revealed by nanoparticle tracking analysis (NTA).

(D) The protein level of CD9, HSP70, TSG101, CD63, and GLG1 of GLG1-NP and CTRL-NP revealed by western blotting.

(E) Organ distribution of Cy5-labeled NP at 4 and 8 h after tail vein injection revealed by biophotonic imaging analysis.

We explored whether the GLG1-NP could promote fracture healing in UC. We established femoral shaft fractures with intramedullary nail fixation in UC mice. They were treated with GLG1-NP intravenously, and the callus was collected at 14 and 21 days postoperatively (Figure S7A). The GLG1-NP increased the calcified callus and promoted fracture union (Figures S7B and S7C). Quantitative analysis validated that the BV/TV in UC mice was elevated by GLG1-NP (Figures S7D and S7E). Meanwhile, GLG1-NP promoted fracture healing in UC mice with elevated maximum load and elasticity modulus (Figures S7F and S7G). Safranin O staining confirmed that GLG1-NP could increase the soft callus area and relative callus mineralization during fracture healing in UC mice (Figures S7H–S7M).

DISCUSSION

Our study indicated that osteoblastic bone formation impairment is crucial to reduced bone mass in IBDs. The BMSCs in UC tended to differentiate into adipocytes rather than osteoblasts, and the bone mass and osteoblastic bone formation decreased dramatically, while the bone marrow adipose tissue accumulation increased. Inspiringly, the bone-targeted GLG1-NP could
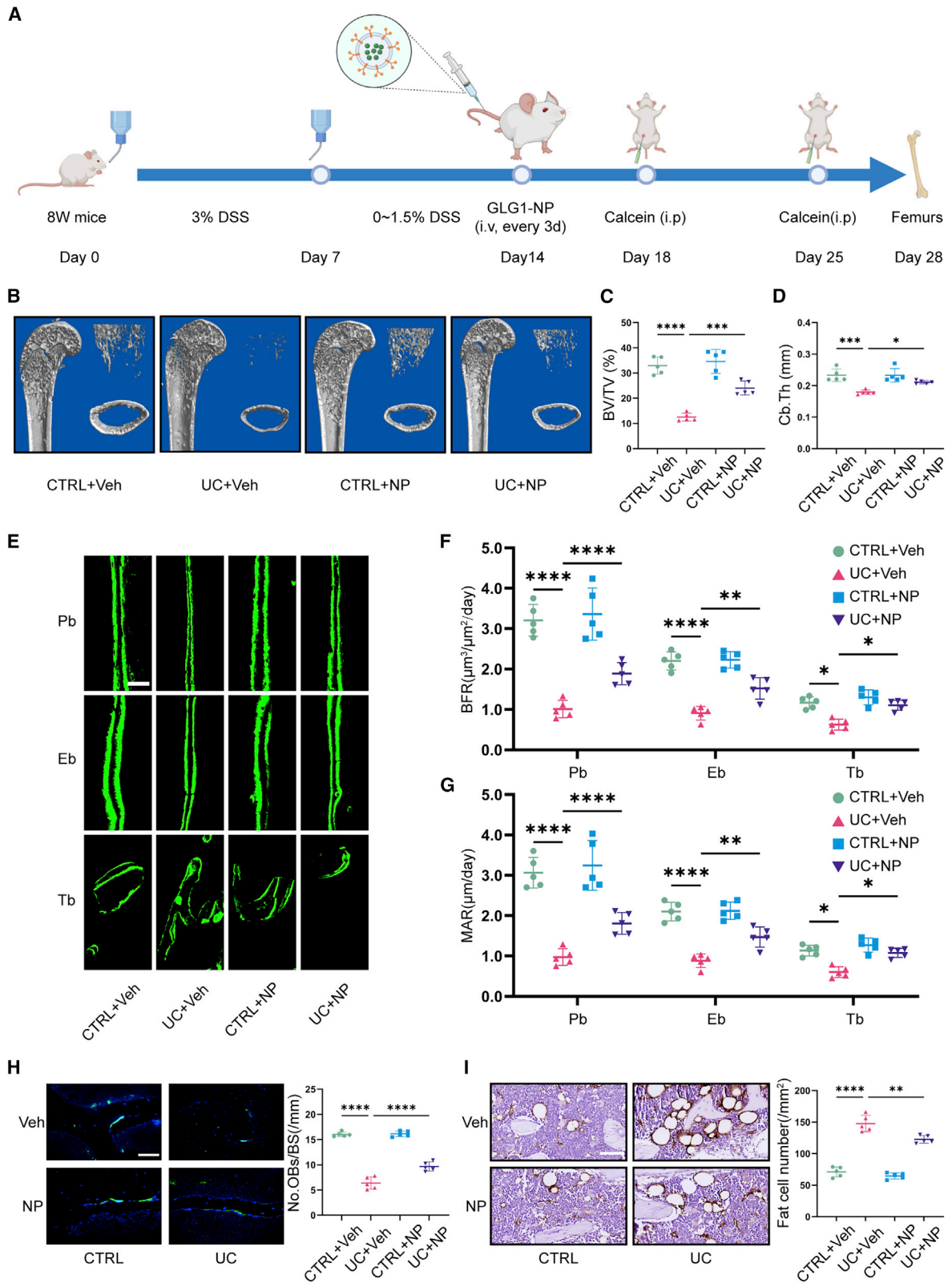
(legend on next page)

regulate BMSC commitment to rescue bone mass reduction and promote fracture healing.

Bone loss could be attributed to accelerated bone remodeling, characterized by the increased number of bone remodeling units coupling osteoclastic bone resorption and osteoblastic bone formation.[44] Despite the widely applied bone resorption inhibitors like bisphosphonates, estrogen and selective estrogen receptor modulators, calcitonin, and cathepsin K inhibitors, bone-forming drugs such as parathormone and teriparatide are emphasized, especially for patients who require sequential therapy with significantly low BMD. Besides, stem cells, microRNA, traditional Chinese medicine, and other bone-targeted therapies also show potential efficacy in dealing with bone loss.[45,46] Recently, inflammatory bone loss in chronic diseases, including obesity, periodontitis, diabetes mellitus, and rheumatoid arthritis, has raised more concern.[47,48] Among them, IBDs are noteworthy as they induce systematic inflammation derived from the intestine.[49,50] Nowadays, IBD has become a global disease with a steadily increased prevalence in Western countries and rapidly increased prevalence in newly industrialized countries.[51,52] Complicated with IBD, bone loss has been discussed for decades.[53] Patients with IBD are susceptible to bone structural defects and increased hip fracture incidence.[54,55] For the pathogenesis, increased inflammation is reported to be responsible.[17,56] To exemplify, bone marrow Th17 TNF-α^+ cells could induce osteoclastogenesis and give rise to excessive bone resorption in IBDs.[57] Also, our TRAP staining verified that overactivated osteoclasts were blamed for inflammatory bone loss.[58,59] For treatment, intervening in the primary diseases and inhibiting inflammation are given priority. Thus, inhibiting immune cells, cytokine, osteoclastogenesis, and osteoclast activity is applicable. Meanwhile, the importance of osteoblastic bone formation is often neglected.[60] However, investigations into the BMSC commitment in IBDs are rare. The bone formation usually coupled with bone resorption will also increase in the context of increased bone resorption. Patients with IBD manifest increased serum levels of bone resorption markers but decreased bone formation, indicating a dysfunctional compensatory bone formation.[61,62] Consistently, we confirmed this in UC models. Several studies emphasized the fracture risk rise in inflammatory bone loss, while its impacts on fracture healing have been poorly understood.[63,64] Our results indicated deteriorative mechanical properties as being the physical basis. Additionally, we observed retarded callus formation and mineralization and compromised fracture union in UC, filling this research gap and raising the importance of ascertaining

bone metabolic changes, especially the osteoblastic bone formation during fracture healing in UC.

Limited evidence is known about bone formation and osteoblastic activity in IBDs.[14,16,65] A rat IBD model induced by 2,4,6-trinitrobenzenesulfonic acid (TNBS) showed that elevated %RANKL$^+$ and %Sclerostin$^+$ osteocytes could predict higher osteoclast surface and lower osteoid surface on cancellous bone, respectively. This highlighted that IBD played a potential role in bone loss by affecting both bone resorption and formation.[15] We found that osteogenesis was markedly inhibited in UC as demonstrated by a calcein double-labeling assay and osteogenic gene expressions. High circulating pro-inflammatory cytokines were proven to impair osteoblastogenesis.[66] Indeed, BMSCs tended to differentiate into adipocytes at the expense of osteoblast generation, causing bone marrow adipose accumulation. This finding also confirmed that chronic inflammation favors adipogenic differentiation rather than osteogenic differentiation of BMSCs, with elevated expression of adipogenic genes like *Pparg*, *Adipoq*, and *Srbp1*.[67–70] Conclusively, the imbalance of bone formation and resorption brings about reduced bone mass. However, inhibiting inflammation could alleviate reduced bone quantity and quality.[71] For mechanisms, we determined the gene transcription changes and several affected signaling pathways in UC. The Wnt/β-catenin pathway crucial to osteoblastic bone formation was significantly downregulated, while the Pparγ pathway vital for adipogenesis was upregulated, explaining BMSC commitment in IBDs.[72] Taken together, suppressed BMSC proliferation and osteogenic differentiation could hardly restore spontaneously and needed effective interventions.

Developing targeting therapies for bone loss in IBDs is necessary as the efficacy of existing biological regimens is debated.[73] Exosome-based bone-targeted NPs have been applied in treating skeletal disorders.[74,75] Our previous study showed that bone-targeted anabolic therapy by CXCR4-based exosome-liposome hybrid NPs could rescue age-related osteoporosis. Specifically, engineered CXCR4$^+$ exosomes loading the antago-miR-188 could specifically accumulate in bone marrow.[35] Similarly, we constructed GLG1-NP to deliver Wnt agonist 1 and successfully promoted bone formation and fracture healing. In summary, medications regulating bone metabolism are indispensable for IBDs, and anabolic therapy should be considered, presenting a promising future in managing inflammatory bone loss.

There were limitations in this study. IBD is a multifactorial challenge with occult pathogenesis among its subtypes. There are several ways to establish IBD models, such as DSS,

Figure 7. GLG1-NP rescued osteoblastic bone formation in UC models

(A) Schematic diagram of UC mice treated by GLG1-NP. The femurs were finally collected on day 28.

(B) Representative µCT reconstruction images of the femurs. Overall view (left), Tb (top right), and cortical bone (bottom right). n = 5.

(C and D) Quantitative analysis of the trabecular and cortical bone revealed by µCT. n = 5.

(E) Representative images of calcein double-labeling assay of Pb, Eb, and Tb of the femurs. n = 5. Scale bar, 50 µm.

(F and G) BFR per bone surface and MAR of the femurs. n = 5.

(H) Immunofluorescence staining of OCN (green) of the femurs. No.OBs/BS as a quantitative measurement. n = 5. Scale bar, 50 µm.

(I) Immunohistochemistry staining of FABP4 (gray) of the femurs. FABP4$^+$ fat cell number as a quantitative measurement. n = 5. Scale bar, 50 µm.

Data are represented as mean ± SD (error bars) from biological replicates. *p < 0.05, **p < 0.01, ***p < 0.001, ****p < 0.0001, by two-way ANOVA and Turkey's multiple comparison test for post hoc analysis.

See also Figures S6 and S7.

trinitrobenzene sulfonic acid, oxazolone, and *IL-10* knockout, but each of these could only partly mimic the pathogenesis in patients with IBD due to the complicated mechanisms. In our study, DSS directly damaged the colonic epithelium and resulted in inflammatory responses throughout the colon. On the other hand, *IL-10*$^{-/-}$ mice developed spontaneous intestinal inflammation characterized by the infiltration of various inflammatory cells, which was further induced by piroxicam.[76,77] We adopted these models to reflect the malfunctions of the mucosal and immune barriers in IBDs, respectively. Our models verified the bone formation alterations in UC, but certain discrepancies in the etiology were calling for further explorations.[60] Undoubtedly, more models would be helpful to conclude more persuasively. Besides, the *in vitro* inflammatory microenvironment simulated by TNF-α treatment could partially reflect the cytokine networks *in vivo*, which were more complicated and required deeper investigations.

To sum up, we unraveled that inhibited osteoblastic bone formation contributed to reduced bone mass and quality in IBDs, and this impairment could be rescued by pharmacological regulation of BMSC fate.

Limitations of the study

The study has several limitations. Firstly, the current study lacks more experimental animal models to illustrate skeletal alterations in Crohn's disease, another subtype of IBD. Secondly, it remains to be determined what is predominant in IBD-related bone loss: the increased bone resorption or decreased bone formation. Thirdly, the clinical exploration of bone metabolism in patients with IBD is limited and should be more comprehensive. To exemplify, bone metabolic parameters could be investigated by analyzing serum samples. However, this requires a sufficient sample size to exclude potential confounding factors and individual discrepancies. Lastly, the immune system involved in inflammatory diseases plays a substantial role in skeletal disorders, calling for further studies to unveil the underlying interactions.

STAR★METHODS

Detailed methods are provided in the online version of this paper and include the following:

- KEY RESOURCES TABLE
- RESOURCE AVAILABILITY
  - Lead contact
  - Materials availability
  - Data and code availability
- EXPERIMENTAL MODEL AND SUBJECT DETAILS
  - Ethics statement
  - Mouse models
  - Piroxicam-accelerated colitis model
  - Medial femoral fracture model
  - Human samples
  - Human serum samples
- METHOD DETAILS
  - μCT analysis
  - Mechanical stress testing
  - Calcein double-labeling assay
  - Quantitative real-time PCR (qRT-PCR) assay
  - Western blotting
  - Fluorescence activated cell sorting (FACS) and RNA sequencing (RNA-seq)
  - Cell culture, von Kossa, ALP, alizarin red s (ARS), and oil red staining
  - Colony-forming unit-fibroblasts (CFU-Fs) assay
  - Histology and histomorphometry
  - Exosome isolation and nanoparticles preparation
- QUANTIFICATION AND STATISTICAL ANALYSIS

AUTHOR CONTRIBUTIONS

J.G., F.W., and Y.H. contributed equally to this work. J.G., F.W., Y.H., Y.L., H.Z., H.L., and S.S. performed the biochemistry and animal studies, analyzed the data, and wrote the manuscript. L.B. and S.L. collected and managed the clinical samples. F.W., Y.H., X.Z., and T.Z. performed the cell biology, morphological, IF, and IHC staining. Y.W., K.X., C.X., X.C., and J.S. conceived and design the project. C.X., X.C., and J.S. supervised the project and provided financial support. All authors read and approved the manuscript.

REFERENCES

1. Hardy, R., and Cooper, M.S. (2009). Bone loss in inflammatory disorders. J. Endocrinol. *201*, 309–320. https://doi.org/10.1677/JOE-08-0568.

2. Merlotti, D., Mingiano, C., Valenti, R., Cavati, G., Calabrese, M., Pirrotta, F., Bianciardi, S., Palazzuoli, A., and Gennari, L. (2022). Bone fragility in gastrointestinal disorders. Int. J. Mol. Sci. *23*, 2713. https://doi.org/10.3390/ijms23052713.

3. Liu, S., Liu, J., Liu, X., Shang, J., Xu, L., Yu, R., and Shui, J. (2021). The microbiome in inflammatory bowel diseases: from pathogenesis to therapy. Nat. Nanotechnol. *16*, 331–336. https://doi.org/10.1007/s13238-020-00745-3.

4. Kaplan, G.G. (2015). The global burden of IBD: from 2015 to 2025. Nat. Rev. Gastroenterol. Hepatol. *12*, 720–727. https://doi.org/10.1038/nrgastro.2015.150.

5. Ye, L., Cao, Q., and Cheng, J. (2013). Review of inflammatory bowel disease in China. Sci. World J. *2013*, 296470. https://doi.org/10.1155/2013/296470.

6. Tilg, H., Moschen, A.R., Kaser, A., Pines, A., and Dotan, I. (2008). Gut, inflammation and osteoporosis: basic and clinical concepts. Gut *57*, 684–694. https://doi.org/10.1136/gut.2006.117382.

7. Rodríguez-Bores, L., Barahona-Garrido, J., and Yamamoto-Furusho, J.K. (2007). Basic and clinical aspects of osteoporosis in inflammatory bowel disease. World J. Gastroenterol. *13*, 6156–6165. https://doi.org/10.3748/wjg.v13.i46.6156.

8. Szafors, P., Che, H., Barnetche, T., Morel, J., Gaujoux-Viala, C., Combe, B., and Lukas, C. (2018). Risk of fracture and low bone mineral density in adults with inflammatory bowel diseases. A systematic literature review with meta-analysis. Osteoporos. Int. *29*, 2389–2397. https://doi.org/10.1007/s00198-018-4586-6.

9. Lamb, C.A., Kennedy, N.A., Raine, T., Hendy, P.A., Smith, P.J., Limdi, J.K., Hayee, B., Lomer, M.C.E., Parkes, G.C., Selinger, C., et al. (2019). British Society of Gastroenterology consensus guidelines on the management of inflammatory bowel disease in adults. Gut *68*, s1–s106. https://doi.org/10.1136/gutjnl-2019-318484.

10. Oliveira, S.B., and Monteiro, I.M. (2017). Diagnosis and management of inflammatory bowel disease in children. BMJ *357*, j2083. https://doi.org/10.1136/bmj.j2083.

11. Eastell, R., and Szulc, P. (2017). Use of bone turnover markers in postmenopausal osteoporosis. Lancet Diabetes Endocrinol. *5*, 908–923. https://doi.org/10.1016/S2213-8587(17)30184-5.

12. Chen, X., Zhi, X., Wang, J., and Su, J. (2018). RANKL signaling in bone marrow mesenchymal stem cells negatively regulates osteoblastic bone formation. Bone Res. *6*, 34. https://doi.org/10.1038/s41413-018-0035-6.

13. Hu, Y., Li, X., Zhi, X., Cong, W., Huang, B., Chen, H., Wang, Y., Li, Y., Wang, L., Fang, C., et al. (2021). RANKL from bone marrow adipose lineage cells promotes osteoclast formation and bone loss. EMBO Rep. *22*, e52481. https://doi.org/10.15252/embr.202152481.

14. Hamdani, G., Gabet, Y., Rachmilewitz, D., Karmeli, F., Bab, I., and Dresner-Pollak, R. (2008). Dextran sodium sulfate-induced colitis causes rapid bone loss in mice. Bone *43*, 945–950. https://doi.org/10.1016/j.bone.2008.06.018.

15. Metzger, C.E., Narayanan, A., Zawieja, D.C., and Bloomfield, S.A. (2017). Inflammatory bowel disease in a rodent model alters osteocyte protein levels controlling bone turnover. J. Bone Miner. Res. *32*, 802–813. https://doi.org/10.1002/jbmr.3027.

16. Dresner-Pollak, R., Gelb, N., Rachmilewitz, D., Karmeli, F., and Weinreb, M. (2004). Interleukin 10-deficient mice develop osteopenia, decreased bone formation, and mechanical fragility of long bones. Gastroenterology *127*, 792–801. https://doi.org/10.1053/j.gastro.2004.06.013.

17. Al Saedi, A., Sharma, S., Bani Hassan, E., Chen, L., Ghasem-Zadeh, A., Hassanzadeganroudsari, M., Gooi, J.H., Stavely, R., Eri, R., Miao, D., et al. (2022). Characterization of skeletal phenotype and associated mechanisms with chronic intestinal inflammation in the winnie mouse model of spontaneous chronic colitis. Inflamm. Bowel Dis. *28*, 259–272. https://doi.org/10.1093/ibd/izab174.

18. Khosla, S., and Hofbauer, L.C. (2017). Osteoporosis treatment: recent developments and ongoing challenges. Lancet Diabetes Endocrinol. *5*, 898–907. https://doi.org/10.1016/S2213-8587(17)30188-2.

19. Li, X., Wang, L., Huang, B., Gu, Y., Luo, Y., Zhi, X., Hu, Y., Zhang, H., Gu, Z., Cui, J., et al. (2020). Targeting actin-bundling protein L-plastin as an anabolic therapy for bone loss. Sci. Adv. *6*, eabb7135. https://doi.org/10.1126/sciadv.abb7135.

20. Estell, E.G., and Rosen, C.J. (2021). Emerging insights into the comparative effectiveness of anabolic therapies for osteoporosis. Nat. Rev. Endocrinol. *17*, 31–46. https://doi.org/10.1038/s41574-020-00426-5.

21. Bernstein, C.N., Targownik, L.E., and Leslie, W.D. (2014). What is the role for bisphosphonates in IBD? Gut *63*, 1369–1370. https://doi.org/10.1136/gutjnl-2013-306141.

22. Wang, L., Huang, B., Chen, X., and Su, J. (2020). New insight into unexpected bone formation by denosumab. Drug Discov. Today *25*, 1919–1922. https://doi.org/10.1016/j.drudis.2020.09.001.

23. Narayanan, S.A., Metzger, C.E., Bloomfield, S.A., and Zawieja, D.C. (2018). Inflammation-induced lymphatic architecture and bone turnover changes are ameliorated by irisin treatment in chronic inflammatory bowel disease. Faseb. J. *32*, 4848–4861. https://doi.org/10.1096/fj.201800178R.

24. Chen, S., Chen, X., Geng, Z., and Su, J. (2022). The horizon of bone organoid: a perspective on construction and application. Bioact. Mater. *18*, 15–25. https://doi.org/10.1016/j.bioactmat.2022.01.048.

25. Chen, J., Li, M., Liu, A.Q., Zheng, C.X., Bao, L.H., Chen, K., Xu, X.L., Guan, J.T., Bai, M., Zhou, T., et al. (2020). Gli1(+) cells couple with type H vessels and are required for type H vessel formation. Stem Cell Rep. *15*, 110–124. https://doi.org/10.1016/j.stemcr.2020.06.007.

26. Salhotra, A., Shah, H.N., Levi, B., and Longaker, M.T. (2020). Mechanisms of bone development and repair. Nat. Rev. Mol. Cell Biol. *21*, 696–711. https://doi.org/10.1038/s41580-020-00279-w.

27. Leppkes, M., and Neurath, M.F. (2020). Cytokines in inflammatory bowel diseases - update 2020. Pharmacol. Res. *158*, 104835. https://doi.org/10.1016/j.phrs.2020.104835.

28. Yang, N., Wang, G., Hu, C., Shi, Y., Liao, L., Shi, S., Cai, Y., Cheng, S., Wang, X., Liu, Y., et al. (2013). Tumor necrosis factor alpha suppresses the mesenchymal stem cell osteogenesis promoter miR-21 in estrogen deficiency-induced osteoporosis. J. Bone Miner. Res. *28*, 559–573. https://doi.org/10.1002/jbmr.1798.

29. Du, D., Zhou, Z., Zhu, L., Hu, X., Lu, J., Shi, C., Chen, F., and Chen, A. (2018). TNF-alpha suppresses osteogenic differentiation of MSCs by accelerating P2Y2 receptor in estrogen-deficiency induced osteoporosis. Bone *117*, 161–170. https://doi.org/10.1016/j.bone.2018.09.012.

30. Russell, T., Watad, A., Bridgewood, C., Rowe, H., Khan, A., Rao, A., Loughenbury, P., Millner, P., Dunsmuir, R., Cuthbert, R., et al. (2021). IL-17A and TNF modulate normal human spinal entheseal bone and soft tissue mesenchymal stem cell osteogenesis, adipogenesis, and stromal function. Cells *10*, 341. https://doi.org/10.3390/cells10020341.

31. Tevlin, R., Seo, E.Y., Marecic, O., McArdle, A., Tong, X., Zimdahl, B., Malkovskiy, A., Sinha, R., Gulati, G., Li, X., et al. (2017). Pharmacological rescue of diabetic skeletal stem cell niches. Sci. Transl. Med. *9*, eaag2809. https://doi.org/10.1126/scitranslmed.aag2809.

32. Xue, X., Hu, Y., Deng, Y., and Su, J. (2021). Recent advances in design of functional biocompatible hydrogels for bone tissue engineering. Adv. Funct. Mater. *31*, 2009432. https://doi.org/10.1002/adfm.202009432.

33. Xue, X., Hu, Y., Wang, S., Chen, X., Jiang, Y., and Su, J. (2022). Fabrication of physical and chemical crosslinked hydrogels for bone tissue engineering. Bioact. Mater. *12*, 327–339. https://doi.org/10.1016/j.bioactmat.2021.10.029.

34. Song, H., Li, X., Zhao, Z., Qian, J., Wang, Y., Cui, J., Weng, W., Cao, L., Chen, X., Hu, Y., and Su, J. (2019). Reversal of osteoporotic activity by endothelial cell-secreted bone targeting and biocompatible exosomes. Nano Lett. *19*, 3040–3048. https://doi.org/10.1021/acs.nanolett.9b00287.

35. Hu, Y., Li, X., Zhang, Q., Gu, Z., Luo, Y., Guo, J., Wang, X., Jing, Y., Chen, X., and Su, J. (2021). Exosome-guided bone targeted delivery of Antagomir-188 as an anabolic therapy for bone loss. Bioact. Mater. *6*, 2905–2913. https://doi.org/10.1016/j.bioactmat.2021.02.014.

36. Liu, H., Zhang, Q., Wang, S., Weng, W., Jing, Y., and Su, J. (2022). Bacterial extracellular vesicles as bioactive nanocarriers for drug delivery: advances and perspectives. Bioact. Mater. *14*, 169–181. https://doi.org/10.1016/j.bioactmat.2021.12.006.

37. Esposito, M., Mondal, N., Greco, T.M., Wei, Y., Spadazzi, C., Lin, S.C., Zheng, H., Cheung, C., Magnani, J.L., Lin, S.H., et al. (2019). Bone vascular niche E-selectin induces mesenchymal-epithelial transition and Wnt activation in cancer cells to promote bone metastasis. Nat. Cell Biol. *21*, 627–639. https://doi.org/10.1038/s41556-019-0309-2.

38. Wang, G., Yuan, J., Cai, X., Xu, Z., Wang, J., Ocansey, D.K.W., Yan, Y., Qian, H., Zhang, X., Xu, W., and Mao, F. (2020). HucMSC-exosomes carrying miR-326 inhibit neddylation to relieve inflammatory bowel disease in mice. Clin. Transl. Med. *10*, e113. https://doi.org/10.1002/ctm2.113.

39. Holgersen, K., Dobie, R., Farquharson, C., van't Hof, R., Ahmed, S.F., Hansen, A.K., and Holm, T.L. (2015). Piroxicam treatment augments bone abnormalities in interleukin-10 knockout mice. Inflamm. Bowel Dis. *21*, 257–266. https://doi.org/10.1097/MIB.0000000000000269.

40. Seul, K.J., Cho, H.S., Heo, S.H., Baek, W.Y., Kim, J.E., Park, E.K., Choi, J.Y., Ryoo, H.M., and Cho, J.Y. (2011). Osteoblast-specific expression of MEF induces osteopenia through downregulation of osteoblastogenesis and upregulation of osteoclastogenesis. J. Bone Miner. Res. *26*, 341–350. https://doi.org/10.1002/jbmr.208.

41. Baek, K., Cho, J.Y., Hwang, H.R., Kwon, A., Lee, H.L., Park, H.J., Qadir, A.S., Ryoo, H.M., Woo, K.M., and Baek, J.H. (2012). Myeloid Elf-1-like factor stimulates adipogenic differentiation through the induction of peroxisome proliferator-activated receptor gamma expression in bone marrow. J. Cell. Physiol. *227*, 3603–3612. https://doi.org/10.1002/jcp.24064.

42. Wang, C., Ning, H., Gao, J., Xue, T., Zhao, M., Jiang, X., Zhu, X., Guo, X., Li, H., and Wang, X. (2022). Disruption of hematopoiesis attenuates the osteogenic differentiation capacity of bone marrow stromal cells. Stem Cell Res. Ther. *13*, 27. https://doi.org/10.1186/s13287-022-02708-3.

43. Chang, J., Liu, F., Lee, M., Wu, B., Ting, K., Zara, J.N., Soo, C., Al Hezaimi, K., Zou, W., Chen, X., et al. (2013). NF-kappaB inhibits osteogenic differentiation of mesenchymal stem cells by promoting beta-catenin degradation. Proc. Natl. Acad. Sci. USA *110*, 9469–9474. https://doi.org/10.1073/pnas.1300532110.

44. Compston, J.E., McClung, M.R., and Leslie, W.D. (2019). Lancet *393*, 364–376. https://doi.org/10.1016/S0140-6736(18)32112-3.

45. Liang, B., Burley, G., Lin, S., and Shi, Y.C. (2022). Osteoporosis pathogenesis and treatment: existing and emerging avenues. Cell. Mol. Biol. Lett. *27*, 72. https://doi.org/10.1186/s11658-022-00371-3.

46. Song, S., Guo, Y., Yang, Y., and Fu, D. (2022). Advances in pathogenesis and therapeutic strategies for osteoporosis. Pharmacol. Ther. *237*, 108168. https://doi.org/10.1016/j.pharmthera.2022.108168.

47. Komatsu, N., and Takayanagi, H. (2022). Mechanisms of joint destruction in rheumatoid arthritis - immune cell-fibroblast-bone interactions. Nat. Rev. Rheumatol. *18*, 415–429. https://doi.org/10.1038/s41584-022-00793-5.

48. de Oliveira, P.G.F.P., Bonfante, E.A., Bergamo, E.T.P., de Souza, S.L.S., Riella, L., Torroni, A., Benalcazar Jalkh, E.B., Witek, L., Lopez, C.D., Zambuzzi, W.F., and Coelho, P.G. (2020). Obesity/metabolic syndrome and diabetes mellitus on peri-implantitis. Trends Endocrinol. Metab. *31*, 596–610. https://doi.org/10.1016/j.tem.2020.05.005.

49. Ke, K., Arra, M., and Abu-Amer, Y. (2019). Mechanisms underlying bone loss associated with gut inflammation. Int. J. Mol. Sci. *20*, 6323. https://doi.org/10.3390/ijms20246323.

50. Zouali, M. (2021). B lymphocytes, the gastrointestinal tract and autoimmunity. Autoimmun. Rev. *20*, 102777. https://doi.org/10.1016/j.autrev.2021.102777.

51. Kaplan, G.G., and Windsor, J.W. (2021). The four epidemiological stages in the global evolution of inflammatory bowel disease. Nat. Rev. Gastroenterol. Hepatol. *18*, 56–66. https://doi.org/10.1038/s41575-020-00360-x.

52. Kaplan, G.G., and Ng, S.C. (2017). Understanding and preventing the global increase of inflammatory bowel disease. Gastroenterology *152*, 313–321.e2. https://doi.org/10.1053/j.gastro.2016.10.020.

53. Zhou, T., Pan, J., Lai, B., Cen, L., Jiang, W., Yu, C., and Shen, Z. (2020). Bone mineral density is negatively correlated with ulcerative colitis: a systematic review and meta-analysis. Clin. Transl. Med. *9*, 18. https://doi.org/10.1186/s40169-020-00270-0.

54. Haschka, J., Hirschmann, S., Kleyer, A., Englbrecht, M., Faustini, F., Simon, D., Figueiredo, C.P., Schuster, L., Muschitz, C., Kocijan, R., et al. (2016). High-resolution quantitative computed tomography demonstrates structural defects in cortical and trabecular bone in IBD patients. J. Crohns Colitis *10*, 532–540. https://doi.org/10.1093/ecco-jcc/jjw012.

55. van Staa, T.P., Cooper, C., Brusse, L.S., Leufkens, H., Javaid, M.K., and Arden, N.K. (2003). Inflammatory bowel disease and the risk of fracture. Gastroenterology *125*, 1591–1597. https://doi.org/10.1053/j.gastro.2003.09.027.

56. Agrawal, M., Arora, S., Li, J., Rahmani, R., Sun, L., Steinlauf, A.F., Mechanick, J.I., and Zaidi, M. (2011). Bone, inflammation, and inflammatory bowel disease. Curr. Osteoporos. Rep. *9*, 251–257. https://doi.org/10.1007/s11914-011-0077-9.

57. Ciucci, T., Ibáñez, L., Boucoiran, A., Birgy-Barelli, E., Pène, J., Abou-Ezzi, G., Arab, N., Rouleau, M., Hébuterne, X., Yssel, H., et al. (2015). Bone marrow Th17 TNFalpha cells induce osteoclast differentiation, and link bone destruction to IBD. Gut *64*, 1072–1081. https://doi.org/10.1136/gutjnl-2014-306947.

58. Chen, Y., Hu, W., Wang, Y., Li, Y., Li, X., Li, H., Tang, Y., Zhang, L., Dong, Y., Yang, X., et al. (2020). A selected small molecule prevents inflammatory osteolysis through restraining osteoclastogenesis by modulating PTEN activity. Clin. Transl. Med. *10*, e240. https://doi.org/10.1002/ctm2.240.

59. Meirow, Y., Jovanovic, M., Zur, Y., Habib, J., Colombo, D.F., Twaik, N., Ashkenazi-Preiser, H., Ben-Meir, K., Mikula, I., Jr., Reuven, O., et al. (2022). Specific inflammatory osteoclast precursors induced during chronic inflammation give rise to highly active osteoclasts associated with inflammatory bone loss. Bone Res. *10*, 36. https://doi.org/10.1038/s41413-022-00206-z.

60. Redlich, K., and Smolen, J.S. (2012). Inflammatory bone loss: pathogenesis and therapeutic intervention. Nat. Rev. Drug Discov. *11*, 234–250. https://doi.org/10.1038/nrd3669.

61. Bischoff, S.C., Herrmann, A., Göke, M., Manns, M.P., von zur Mühlen, A., and Brabant, G. (1997). Altered bone metabolism in inflammatory bowel disease. Am. J. Gastroenterol. *92*, 1157–1163.

62. Silvennoinen, J., Risteli, L., Karttunen, T., and Risteli, J. (1996). Increased degradation of type I collagen in patients with inflammatory bowel disease. Gut *38*, 223–228. https://doi.org/10.1136/gut.38.2.223.

63. Ludvigsson, J.F., Mahl, M., Sachs, M.C., Björk, J., Michaelsson, K., Ekbom, A., Askling, J., Backman, A.S., and Olén, O. (2019). Fracture risk in patients with inflammatory bowel disease: a nationwide population-based cohort study from 1964 to 2014. Am. J. Gastroenterol. *114*, 291–304. https://doi.org/10.14309/ajg.0000000000000062.

64. Ahn, H.J., Kim, Y.J., Lee, H.S., Park, J.H., Hwang, S.W., Yang, D.H., Ye, B.D., Byeon, J.S., Myung, S.J., Yang, S.K., et al. (2022). High risk of fractures within 7 Years of diagnosis in asian patients with inflammatory bowel diseases. Clin. Gastroenterol. Hepatol. *20*, e1022–e1039. https://doi.org/10.1016/j.cgh.2021.06.026.

65. Uluçkan, Ö., Jimenez, M., Karbach, S., Jeschke, A., Graña, O., Keller, J., Busse, B., Croxford, A.L., Finzel, S., Koenders, M., et al. (2016). Chronic skin inflammation leads to bone loss by IL-17-mediated inhibition of Wnt signaling in osteoblasts. Sci. Transl. Med. *8*, 330ra37. https://doi.org/10.1126/scitranslmed.aad8996.

66. Abdelmagid, S.M., Barbe, M.F., and Safadi, F.F. (2015). Role of inflammation in the aging bones. Life Sci. *123*, 25–34. https://doi.org/10.1016/j.lfs.2014.11.011.

67. Munir, H., Ward, L.S.C., Sheriff, L., Kemble, S., Nayar, S., Barone, F., Nash, G.B., and McGettrick, H.M. (2017). Adipogenic differentiation of mesenchymal stem cells alters their immunomodulatory properties in a tissue-specific manner. Stem Cell. *35*, 1636–1646. https://doi.org/10.1002/stem.2622.

68. Osorio, E.Y., Gugala, Z., Patterson, G.T., Palacios, G., Cordova, E., Uscanga-Palomeque, A., Travi, B.L., and Melby, P.C. (2022). Inflammatory stimuli alter bone marrow composition and compromise bone health in the malnourished host. Front. Immunol. *13*, 846246. https://doi.org/10.3389/fimmu.2022.846246.

69. da Silva, S.V., Renovato-Martins, M., Ribeiro-Pereira, C., Citelli, M., and Barja-Fidalgo, C. (2016). Obesity modifies bone marrow microenvironment and directs bone marrow mesenchymal cells to adipogenesis. Obesity 24, 2522–2532. https://doi.org/10.1002/oby.21660.

70. Noack, C., Hempel, U., Preissler, C., and Dieter, P. (2015). Prostaglandin E2 impairs osteogenic and facilitates adipogenic differentiation of human bone marrow stromal cells. Prostaglandins Leukot. Essent. Fatty Acids 94, 91–98. https://doi.org/10.1016/j.plefa.2014.11.008.

71. Tian, J., Chung, H.K., Moon, J.S., Nga, H.T., Lee, H.Y., Kim, J.T., Chang, J.Y., Kang, S.G., Ryu, D., Che, X., et al. (2022). Skeletal muscle mitoribosomal defects are linked to low bone mass caused by bone marrow inflammation in male mice. J. Cachexia Sarcopenia Muscle 13, 1785–1799. https://doi.org/10.1002/jcsm.12975.

72. Li, Y., Jin, D., Xie, W., Wen, L., Chen, W., Xu, J., Ding, J., and Ren, D. (2018). PPAR-Gamma and Wnt regulate the differentiation of MSCs into adipocytes and osteoblasts respectively. Curr. Stem Cell Res. Ther. 13, 185–192. https://doi.org/10.2174/1574888X12666171012141908.

73. Soós, B., Szentpétery, Á., Raterman, H.G., Lems, W.F., Bhattoa, H.P., and Szekanecz, Z. (2022). Effects of targeted therapies on bone in rheumatic and musculoskeletal diseases. Nat. Rev. Rheumatol. 18, 249–257. https://doi.org/10.1038/s41584-022-00764-w.

74. Cui, Y., Guo, Y., Kong, L., Shi, J., Liu, P., Li, R., Geng, Y., Gao, W., Zhang, Z., and Fu, D. (2022). A bone-targeted engineered exosome platform delivering siRNA to treat osteoporosis. Bioact. Mater. 10, 207–221. https://doi.org/10.1016/j.bioactmat.2021.09.015.

75. Jiang, Y., Li, J., Xue, X., Yin, Z., Xu, K., and Su, J. (2022). Engineered extracellular vesicles for bone therapy. Nano Today 44, 101487. https://doi.org/10.1016/j.nantod.2022.101487.

76. Kiesler, P., Fuss, I.J., and Strober, W. (2015). Experimental models of inflammatory bowel diseases. Cell. Mol. Gastroenterol. Hepatol. 1, 154–170. https://doi.org/10.1016/j.jcmgh.2015.01.006.

77. Wirtz, S., Popp, V., Kindermann, M., Gerlach, K., Weigmann, B., Fichtner-Feigl, S., and Neurath, M.F. (2017). Chemically induced mouse models of acute and chronic intestinal inflammation. Nat. Protoc. 12, 1295–1309. https://doi.org/10.1038/nprot.2017.044.

78. Lee, R.H., Yu, J.M., Foskett, A.M., Peltier, G., Reneau, J.C., Bazhanov, N., Oh, J.Y., and Prockop, D.J. (2014). TSG-6 as a biomarker to predict efficacy of human mesenchymal stem/progenitor cells (hMSCs) in modulating sterile inflammation in vivo. Proc. Natl. Acad. Sci. USA 111, 16766–16771. https://doi.org/10.1073/pnas.1416121111.

STAR★METHODS

KEY RESOURCES TABLE

REAGENT or RESOURCE	SOURCE	IDENTIFIER
Antibodies		
Anti-mouse OCN	Abcam	Cat# ab93876; RRID:AB_10675660
Anti-mouse OSTERIX	Abcam	Cat# ab209484; RRID:AB_2892207
Anti-mouse FABP4	Proteintech	21613-1-AP
Anti-mouse ADIPOQ	Abcam	Cat# ab92501; RRID:AB_10562486
Anti-mouse LY6A/E	Biolegend	108108
Anti-mouse CD29	Biolegend	102206
Anti-mouse CD45	Biolegend	103132
Anti-mouse CD11b	Biolegend	101226
Anti-mouse CD9	Abcam	Cat# ab263019
Anti-mouse HSP70	Abcam	Cat# ab181606; RRID:AB_2910093
Anti-mouse TSG 101	Abcam	Cat# ab125011; RRID:AB_10974262
Anti-mouse CD63	Abcam	Cat# ab134045; RRID:AB_2800495
Anti-mouse GLG1	Abcam	Cat# ab271182
Anti-mouse β-catenin	Proteintech	51067-2-AP
Anti-mouse p50	Abcam	Cat# ab32360; RRID:AB_776748
Anti-mouse p-p50	Abcam	Cat# ab28849; RRID:AB_881293
Anti-mouse IKKβ	Abcam	Cat# ab124957; RRID:AB_10975710
Anti-mouse p-IKKβ	Affinity	AF3013
Anti-mouse LaminB1	Abcam	Cat# ab133741; RRID:AB_2616597
Anti-mouse Tubulin	Abcam	Cat# ab179513
Anti-mouse GAPDH	Abcam	Cat# ab181602; RRID:AB_2630358
Anti-rabbit IgG (H&L) (DyLight^{TM} 800 4X PEG Conjugate)	Cell Signaling Technology	Cat# 5151; RRID:AB_10697505
Anti-Rabbit IgG H&L (HRP Conjugated)	Abcam	Cat# ab6721; RRID:AB_955447
Anti-Rabbit IgG H&L (Alexa Fluor® 488)	Abcam	Cat# ab150077; RRID:AB_2630356
Biological samples		
Murine bone marrow mesenchymal stromal/stem cells	Mice in this study	N/A
Human bone marrow mesenchymal stromal/stem cells	Patients in this study	N/A
Human serum	Patients and healthy volunteer in this study	N/A
Chemicals, peptides, and recombinant proteins		
Dextran sulfate sodium (*M.Wt* 36,000–50,000)	MP Biomedicals	9011-18-1
Piroxicam	Sigma-Aldrich	P5654
4% paraformaldehyde buffer	Servicebio	G1101
EDTA (*pH* = 8.0)	Servicebio	G1105
Calcein	Sigma-Aldrich	C0875
TRIzol reagent	Sigma-Aldrich	15596–018
SYBR Green	TaKaRa	RR420A
Phosphate buffer solution	Servicebio	G4202
Alizarin Red S Solution	Solarbio	G1450
Crystal violet staining solution	Beyotime	C0121
EDTA (*pH* = 7.4)	Thermo Fisher	E478-500

(Continued on next page)

Continued

REAGENT or RESOURCE	SOURCE	IDENTIFIER
Dulbecco's Modified Eagle's Medium	Corning	10-013-CV
Fetal bovine serum	Gibco	10099141C
Penicillin-streptomycin	Gibco	5070063
Wnt agonist 1	Selleck	S8178
PEG300	Selleck	S6704
Tween 80	Selleck	S6702
Critical commercial assays		
PrimeScript™ RT reagent Kit	TaKaRa	RR047A
ProteoPrep® Total Extraction Sample Kit	Sigma-Aldrich	PROTTOT
*mir*Vana™ miRNA Isolation Kit	Thermo Fisher	AM1561
TruSeq Stranded mRNA Library Prep Kit	Illumina	20020595
Metal Enhanced DAB Substrate Kit	Solarbio	DA1016
Mouse BMSC complete medium	Cyagen	MUXMX-90011
Mouse osteogenic differentiation medium	Cyagen	MUXMX-90021
Mouse adipogenic differentiation medium	Cyagen	MUXMX-90031
Human BMSC complete medium	Cyagen	HUXMA-90011
Human osteogenic differentiation medium	Cyagen	HUXMA-90021
Human adipogenic differentiation medium	Cyagen	HUXMA-90031
von Kossa Staining Kit	Solarbio	G3282
BCIP/NBT Alkaline Phosphatase Color Development Kit	Beyotime	C3206
Oil Red O staining kit	Solarbio	G1262
Safranin O staining kit	Solarbio	S8020
H&E staining kit	Solarbio	G1120
TRAP staining kit	Whatman	PMC-AK04F-COS
Goldner's trichome staining kit	Solarbio	G3550
Deposited data		
RNA-seq data	This paper	Database: https://www.ncbi.nlm.nih.gov; Project number: SRR18516509-SRR18516514
Experimental models: Cell lines		
NIH/3T3	Cell Bank of the Chinese Academy of Science	GNM 6
GLG1-overexpressed NIH/3T3	OBiO Technology	N/A
Experimental models: Organisms/strains		
Balb/c mice	Vital River Laboratories	211
IL-10$^{-/-}$ mice (Balb/c)	Shanghai Model Organisms Center	NM-KO-200637
Oligonucleotides		
Primer used, see Table S1	Sangon Biotech	N/A
Software and algorithms		
Microsoft office	Microsoft	https://www.microsoft.com/zh-cn/microsoft-365/microsoft-office
SPSS statistics 26.0	IBM	https://www.ibm.com/cn-zh/products/spss-statistics
GraphPad Prism 9.0	GraphPad	http://www.graphpad-prism.cn/
Adobe Photoshop	Adobe	https://www.adobe.com/cn/products/photoshop.html
Adobe Illustrator	Adobe	https://www.adobe.com/cn/products/illustrator.html

RESOURCE AVAILABILITY

Lead contact
Further information and requests for resources and reagents should be direct to and will be fulfilled by the lead contact, Jiacan Su (drsujiacan@163.com).

Materials availability
All unique/stable reagents generated in this study are accessible from the lead contact with a completed Materials Transfer Agreement.

Data and code availability
- RNA-seq data supporting the findings of this study are openly available at NCBI (https://www.ncbi.nlm.nih.gov), referring to SRR18516509-SRR18516514.
- This paper does not generate the original code. All data associated with this study are presented in the paper or supplemental information.
- Any additional information required to reanalyze the data reported in this paper is available from the lead contact upon request.

EXPERIMENTAL MODEL AND SUBJECT DETAILS

Ethics statement
The experiments involving animals or humans were approved by Ethics Committee of Shanghai University (Approval No. ECSHU 2021–146). Patients and/or the public were not involved in the design, conduct, reporting, or dissemination plans of this research. All patients and healthy volunteers signed a consent form approved by the local institutional review board.

Mouse models
DSS-induced acute/chronic colitis models
6-week male Balb/c mice were bought from the Vital River Laboratories (Beijing, China) and the male $IL-10^{-/-}$ mice and their littermates in Balb/c background were constructed and provided by Shanghai Model Organisms Center (Shanghai, China). Those mice were maintained at the density of 5 mice per cage in a standard SPF facility at Shanghai University. The environmental conditions of temperature, humidity, and light-dark cycle were 20–24°C, 40–50%, and 12 h, respectively. For the UC model induced by $M.Wt$ 36,000–50,000 dextran sulfate sodium (DSS) (MP Biomedicals, 9011-18-1), 3% DSS was solvated in the drinking water and replaced every two days. After one week, the concentration was adjusted daily to 0–1.5% to maintain a mild to moderate inflammation according to the DAI, which was determined by hematochezia, weight loss, and feces properties. For each item, the score ranged from 0–4, which was positively correlated with the severity. Then the grade of intestinal inflammation was defined as severe (8–12), moderate (4–8), and mild (0–4) depending on the total DAI score. The DAI was evaluated at the same time point every day since the experiment began. This dynamic adjustment lasted until the end of the experiment, while the control group was fed with freshwater. The chronic UC model was established by DSS described above, with a dynamic change of concentration from day 8 to day 28.

Piroxicam-accelerated colitis model
For the $IL-10^{-/-}$ model, piroxicam (Sigma-Aldrich, P5654) was mixed in the diet of $IL-10^{-/-}$ mice at the dose of 200 ppm for two weeks.

Medial femoral fracture model
For the fracture model, mice were anesthetized by 4% chloral hydrate, and the left femur was cut using a fretsaw, then fixed by an intramedullary nail.

Human samples
Human BMSC
Human BMSC was isolated from bone marrow when the healthy fractured patients underwent internal fixation surgery. The recruited patients were young adults who suffered from accidental trauma, without basic diseases and long-term drug administration before. Then the BMSC within the bone marrow was obtained and purified by serial passages.[78] Bone-marrow aspirates from humans were cultured in a complete medium (Cyagen, HUXMA-90011) to obtain adherent cells (90% confluency, P0 cells). They were replated at a low density (70 cells per cm^{-2}) to obtain P1 cells (70% confluency). The P1 cells could be divided and preserved using liquid nitrogen. Those cells were thawed and cultured with a high density and then replated at a low density to obtain P2 cells, which were used to perform the following experiments.

Human serum samples

For the human serum collections, the male and female patients who participated in our study followed the criteria: Aged 18 to 65, first diagnosed as UC by two chief physicians in the department of gastroenterology (according to the evidence of radiology, endoscopy, and histology). The exclusive criteria were listed as follows: Severe systematic diseases such as cardiopulmonary malfunction, hepatic or renal functional abnormality, and hypogonadism or thyrotoxicosis. Metabolic syndrome including diabetes and obesity. Skeletal disorders such as ankylosing spondylitis and rheumatoid arthritis. History of drug or toxicant administration that might affect bone metabolism, exemplified by bisphosphates, calcium, vitamin D, calcitonin, glucocorticoids, hormones, biological agents, and traditional Chinses medicine. Pregnancy, malnutrition, and malabsorption are also excluded. The healthy volunteers were invited meeting the criteria that aged 18 to 65 and without any systematic diseases or drug history.

METHOD DETAILS

µCT analysis

Femurs from mice were used for microcomputed tomography (µCT) (Bruker, Skyscan 1275) examination. Image acquisition was performed at 50 kV and 60 µA using 11 µm resolution. For the scan of bone marrow adipose tissue, the femurs were fixed in 4% para-formaldehyde buffer (Servicebio, G1101) for 2 days and decalcified in 0.5 mmol L^{-1} EDTA (pH = 8.0, Servicebio, G1105) for 21 days. Then their proximal parts were discarded. The distal parts were immersed in an aqueous solution dissolved osmium tetroxide (1%) and potassium dichromate (2.5%) for a two-day incubation in a fume cupboard. Rinse them with tap water for 2 h before the scan. Image acquisition was performed at 50 kV and 60 µA using 7 µm resolution. The three-dimensional stereogram was reconstructed by CTvox and the cortical and cancellous bone analysis parameters were analyzed by CTAn.

Mechanical stress testing

Right femurs from mice were collected to undergo the three-point femur bending tests. After the isolation, femurs were fixed in 75% ethanol. Three-point femur bending tests were set with a support span of 7 mm and a vertical loading speed of 0.02 mm s^{-1}. Acumen® Electrodynamic Test Systems (MTS, Acumen 3) was used to test the maximum axial force the femurs could be sustained, as well as their elasticity modulus.

Calcein double-labeling assay

Mice were intraperitoneally injected with 1 mg mL^{-1} calcein (8 mg kg^{-1}, Sigma-Aldrich, C0875) at 10 and 3 days before sacrifice. Femurs were detached from the tissue and sections were prepared without decalcification and underwent hard-tissue slicing. The images were observed by a fluorescence microscope. Mineral apposition rate (MAR) and bone formation rate (BFR) were regarded as the parameters of bone formation.

Quantitative real-time PCR (qRT-PCR) assay

The total RNA isolation was achieved by the TRIzol reagent (Sigma-Aldrich, 15596–018). The concentration of RNA was measured at OD260. The cDNA was obtained by extracted RNA by reverse transcription, using PrimeScript™ RT reagent Kit (TaKaRa, RR047A). SYBR Green (TaKaRa, RR420A) was applied to proceed with qRT-PCR following the manufacturer's instructions. Mouse and human *Gapdh* was set as the internal housekeeping gene, respectively. Gene transcriptional changes were analyzed by the $2^{-\triangle\triangle Ct}$ method. Each datum plotted in the figure represented the average value of three technical replicates. The primer sequences are provided in Table S1.

Western blotting

Protein extraction was conducted from bone tissue or BMSC using ProteoPrep® Total Extraction Sample Kit (Sigma-Aldrich, PROTTOT) following the manufacturer's instructions. Polyvinylidene fluoride (PVDF) membrane was used to immobilize and block the separated proteins. The primary antibodies and dilution ratio are listed in Table S2. Anti-rabbit IgG (H&L) (DyLight™ 800 4X PEG Conjugate, Cell Signaling Technology, 5151) was employed as a secondary antibody with a dilution rate of 1:20,000. Then the coloration reaction was completed by Metal Enhanced DAB Substrate Kit (Solarbio, DA1016)

Fluorescence activated cell sorting (FACS) and RNA sequencing (RNA-seq)

Bone marrow was isolated by rinsing the femoral cavity of 8-week male control and UC mice. Use a cellular strainer to remove impurities from the bone marrow rinse. 1.2 million cells were resuspended with phosphate buffer solution (PBS, Servicebio, G4202) and evenly distributed into 6 EP tubes. Add 1 µL cytometry antibody for every 200,000 cells. Each EP tube added no antibody, Ly6A/E (1 µL), CD29 (1 µL), CD45 (1 µL), CD11b (1 µL), and four antibodies (4 µL in total). (Table S2) Incubate in the dark for 15 min. Cells were centrifuged at 160 ×*g* for 10 min and sediment was kept. Cells were resuspended with 200 µL PBS to repeat this procedure. Then the cells were resuspended with 200 µL PBS and sorted by a high-speed sorting flow cytometer (Beckman Coulter, MoFlo XDP) to calibrate the sorting gate. The other cells were incubated with four antibodies according to the method above. Then the collected cells underwent transcriptome sequencing by OE Biotech (Shanghai, China).

For RNA-seq, we used the *mir*Vana™ miRNA Isolation Kit (Thermo Fisher, AM1561) following the manufacturer's protocol to extract the total RNA. Its integrity was evaluated by a bioanalyzer (Agilent, Agilent 2100). Those with RNA Integrity Number (RIN) $\geq$ 7 were reserved for the subsequent experiments. The libraries were established by TruSeq Stranded mRNA Library Prep Kit (Illumina, 20020595) following the instructions within the kit. Next, they were sequenced on the sequencing platform (Illumina, HiSeq 2500) and 125bp/150bp paired-end reads were generated.

Cell culture, von Kossa, ALP, alizarin red s (ARS), and oil red staining

Bone marrow from the femurs of 8-week male control and UC mice was harvested to obtain BMSC.[78] We isolated the lower limbs and detached the soft tissues under the sterile circumstance. The distal and proximal femur were discarded to wash out the bone marrow with a 1-mL syringe containing PBS. The cells within the rinse were washed with PBS and then cultured in a mouse complete medium (Cyagen, MUXMX-90011).

For von Kossa, ALP, and ARS staining, BMSC was cultured in a mouse osteogenic differentiation medium (Cyagen, MUXMX-90021). After 2 weeks, cells were fixed for 20 min using 4% paraformaldehyde and performed von Kossa, ALP, and ARS staining using von Kossa Staining Kit (Solarbio, G3282), BCIP/NBT Alkaline Phosphatase Color Development Kit (Beyotime, C3206), and Alizarin Red S Solution (Solarbio, G1450) following manuals. For oil red staining, BMSC were cultured in a mouse adipogenic differentiation medium (Cyagen, MUXMX-90031). After 3 weeks, cells were fixed by the methods aforementioned and performed oil red staining using Oil Red O staining kit (Solarbio, G1262). The images were taken by an imaging reader (BioTek, Cytation 5).

For human sample management, peripheral blood from the health volunteers and UC patients was harvested using vacuum tubes. The samples were rested for 2 h. Then the serum samples were collected in a sterile tube and centrifuged at 1500 ×*g* for 15 min. Then the reserved supernatant was added (10%, *v/v*) to the human basal medium (Cyagen, HUXMA-90011) for cell culture. The osteogenic and adipogenic induction was performed similarly by adding human samples to a human inducible medium (Cyagen, HUXMA-90021, HUXMA-90031) for 7 days, respectively.

Colony-forming unit-fibroblasts (CFU-Fs) assay

BMSC obtained from the bone marrow of control and UC mice were seeded in six-well plates (10,000 per well). After being cultured in a complete medium (Cyagen, MUXMX-90011) for 7 days, BMSC were fixed by the methods aforementioned and performed crystal violet staining solution (Beyotime, C0121) for 1/4 h, then washed with PBS. The images were taken by an imaging reader (BioTek, Cytation 5).

Histology and histomorphometry

Bone samples were immersed in 4% paraformaldehyde after being isolated from mice, then decalcified in 10% EDTA (*pH* = 7.4, Thermo Fisher, E478-500) for 21 days and embedded in paraffin to prepare slices for staining. Similarly, the colon, heart, liver, spleen, lung, and kidney of the mice were treated with 4% paraformaldehyde and embedded in paraffin. The paraffin slides were incubated at 37°C overnight, then dewaxed and rehydrated through gradient ethanol into the water for the subsequent experiments.

Safranin O (Solarbio, S8020), H&E (Solarbio, G1120), TRAP (Whatman, PMC-AK04F-COS), and Goldner's trichome (Solarbio, G3550) staining were then performed to evaluate various parameters according to corresponding staining kit.

The slices were treated with PBS with goat serum (10%) and Triton-X-100 (0.1%) for 0.5h after retrieving with sodium citrate antigen retrieval solution (Solarbio, C1031) at 95°C for 15 min. For IHC staining, the slices were treated by primary antibodies at 4°C for 12 h. After being rinsed with PBS, the slides were treated by Goat Anti-Rabbit IgG H&L (HRP Conjugated, Abcam, ab6721) for 60 min with a dilution of 1:1,000. Then the coloration reaction was completed by Metal Enhanced DAB Substrate Kit (Solarbio, DA1016). For IF staining, the slices were stained with DAPI for 10 s after Goat Anti-Rabbit IgG H&L (Alexa Fluor® 488, Abcam, ab150077) treatment, with a dilution ratio of 1:1,000. Images were taken and analyzed by a fluorescence microscope.

The primary antibodies are listed in Table S2.

Exosome isolation and nanoparticles preparation

NIH/3T3 cell line was bought from the Cell Bank of the Chinese Academy of Science (Shanghai, China). The overexpression of GLG1 in the NIH/3T3 cell line was completed by OBiO Technology (Shanghai, China). They were cultured on a 10-cm petri dish with the supplement of high-glucose Dulbecco's Modified Eagle's Medium (Corning, 10-013-CV) with 10% (*v/v*) fetal bovine serum (Gibco, 10099141C) and 100 µg mL^{-1} penicillin-streptomycin (Gibco, 5070063) at 37°C in 5% CO_2 humidified incubator. When the cells confluence reached 50%, the previous medium was replaced by that with exosome-free fetal bovine serum, which was prepared by ultracentrifugation at 110,000 ×*g* for 70 min. After 24 h, the supernatant was harvested for gradient centrifugation and finally exosomes were obtained. The supernatant underwent 2,000 ×*g* centrifugation (5 min), 10,000 ×*g* centrifugation (1 h), and 110,000 ×*g* ultracentrifugation (70 min) to collect the sediment at last. Then the sediment was resuspended with 1 mL PBS and underwent 110,000×*g* ultracentrifugation (70 min) for washing to obtain exosomes in the sediment, which was resuspended by 100 µL PBS. The exosomes were stored at −80°C within 30 days for the following experiments. Wnt agonist 1 (S8178) was purchased from Selleck (Shanghai, China). Then it was dissolved successively by 2% DMSO, 40% PEG300 (S6704), 2% Tween 80 (S6702), and double distilled water. 1 mL mixture of exosomes (200 µg protein equivalent) and Wnt agonist 1 was loaded in a mini extruder (Avanti Polar Lipids, 610000) and loaded with a 100-µm polycarbonate membrane (Avanti Polar Lipids, 610005) for twenty extrusion cycles. The

following detections of NP were described in our previous work.[35] Finally, the GLG1-NP was injected intravenously with the dosage equivalent to 5 mg kg^{-1} Wnt agonist 1. Meanwhile, equivalent GLG1$^+$ exosomes containing vehicle were used as the control treatment.

QUANTIFICATION AND STATISTICAL ANALYSIS

All data were presented as mean ± SD or mean ± SEM, which was indicated in the figure legends. IBM SPSS statistics 26.0 was applied for statistical analysis. For a single comparison, an unpaired or paired Student's t-test was applied. And for the multiple comparisons between groups, a two-way analysis of variance (ANOVA) with Tukey's post hoc test was used. $P<0.05$ was set as the statistically significant criterion. Figures were generated in GraphPad Prism 9.0. Then the image processing and assembly were accomplished by Adobe Photoshop and Adobe Illustrator.